Research Paper

GEOSPHERE

GEOSPHERE, v. 17, no. 3

https://doi.org/10.1130/GES02211.1

13 figures; 2 tables; 1 set of supplemental files

CORRESPONDENCE: pzhougeology@gmail.com

CITATION: Zhou, P., Ireland, T., Murray, R.W., and Clift, P.D., 2021, Marine sedimentary records of chemical weathering evolution in the western Himalaya since 17 Ma: Geosphere, v. 17, no. 3, p. 824–853, https://doi.org/10.1130/GES02211.1.

Science Editor: David E. Fastovsky
Associate Editor: Rhawn Denniston

Received 11 November 2019
Revision received 14 October 2020
Accepted 29 January 2021

Published online 24 March 2021

Marine sedimentary records of chemical weathering evolution in the western Himalaya since 17 Ma

Peng Zhou[1], Thomas Ireland[2], Richard W. Murray[3], and Peter D. Clift[1,4]

[1]Department of Geology and Geophysics, Louisiana State University, Baton Rouge, Louisiana 70803, USA
[2]Department of Earth and Environment, Boston University, Boston, Massachusetts 02215, USA
[3]Woods Hole Oceanographic Institution, Woods Hole, Massachusetts 02543, USA
[4]Research Center for Earth System Science, Yunnan University, Kunming, Yunnan 650091, China

ABSTRACT

The Indus Fan derives sediment from the western Himalaya and Karakoram. Sediment from International Ocean Discovery Program drill sites in the eastern part of the fan coupled with data from an industrial well near the river mouth allow the weathering history of the region since ca. 16 Ma to be reconstructed. Clay minerals, bulk sediment geochemistry, and magnetic susceptibility were used to constrain degrees of chemical alteration. Diffuse reflectance spectroscopy was used to measure the abundance of moisture-sensitive minerals hematite and goethite. Indus Fan sediment is more weathered than Bengal Fan material, probably reflecting slow transport, despite the drier climate, which slows chemical weathering rates. Some chemical weathering proxies, such as K/Si or kaolinite/(illite + chlorite), show no temporal evolution, but illite crystallinity and the chemical index of alteration do have statistically measurable decreases over long time periods. Using these proxies, we suggest that sediment alteration was moderate and then increased from 13 to 11 Ma, remained high until 9 Ma, and then reduced from that time until 6 Ma in the context of reduced physical erosion during a time of increasing aridity as tracked by hematite/goethite values. The poorly defined reducing trend in weathering intensity is not clearly linked to global cooling and at least partly reflects regional climate change. Since 6 Ma, weathering has been weak but variable since a final reduction in alteration state after 3.5 Ma that correlates with the onset of Northern Hemispheric glaciation. Reduced or stable chemical weathering at a time of falling sedimentation rates is not consistent with models for Cenozoic global climate change that invoke greater Himalayan weathering fluxes drawing down atmospheric CO_2 but are in accord with the idea of greater surface reactivity to weathering.

INTRODUCTION

Chemical weathering is responsible for the breakdown of bedrock and its transformation into soil and subsequently into fluvial and marine sediment. This process has important feedbacks to global climate because breakdown of silicate minerals consumes CO_2 (Berner and Berner, 1997). CO_2 is a well-known greenhouse gas that has been linked to long-term global cooling during the Cenozoic (Berner and Berner, 1997). Rates of chemical weathering are largely controlled by humidity and temperature, particularly at high erosion rates (Kump et al., 2000; West et al., 2005), and therefore should be linked to the intensity of the Asian summer monsoon. If the long-term cooling of the planet during the Cenozoic is caused by increased chemical weathering fluxes, then this should be reflected in the sediment record, especially in the Asian marginal seas because the uplift of high topography in Asia has been cited as the primary cause for the increased erosion and weathering during that time (Raymo and Ruddiman, 1992). More recently, it has been argued that it is preferential chemical weathering of low-latitude mafic arc complexes that has provided the additional weathering flux, rather than erosion of the Himalaya themselves (Jagoutz et al., 2016; Macdonald et al., 2019). Furthermore, others have argued that CO_2 drawdown is a product not of increased total weathering flux, but rather of increase in the strength of silicate weathering feedbacks (Caves et al., 2016). In this scenario, increases in rock reactivity during the Cenozoic are the critical control, an argument recently supported by modeling that attempted to explain increasing seawater $^{7}Li/^{6}Li$ values that are suggested to track silicate weathering intensity, while accounting for constant seawater $^{10}Be/^{9}Be$ values that document ocean-basin silicate weathering flux (Caves Rugenstein et al., 2019). Our work is designed to directly measure the chemical weathering history of the western Himalaya based on the composition of the eroded products for the first time, rather than inferring this from an oceanic water proxy record. Proxies that estimate global fluxes from seawater chemistry are commonly globally integrated averages and, as a result, are unable to pinpoint those areas that are most active and simply indicate that the total is going up or down. By looking at the Indus Fan and thus only the western Himalaya, we should be able to test the original hypothesis of Raymo and Ruddiman (1992) that links uplift of the Tibetan plateau, weathering of sediment eroded from the Himalayan mountains, and the subsequent feedback to global climate.

In this study, we use sediment cores recovered from the eastern Arabian Sea (International Ocean Discovery Program [IODP] Sites U1456 and U1457) to examine the history of chemical weathering in the western Himalaya. Cores penetrating the upper Miocene provide an erosion and weathering record

Peng Zhou https://orcid.org/0000-0001-8661-1942

stretching back almost 11 m.y., which can then be compared with existing climatic and oceanographic records in order to determine possible controlling mechanisms of chemical weathering. We extend this record further back in time by integrating samples dating back to ca. 17 Ma from an industrial borehole on the Indus continental shelf, Indus Marine A-1, drilled by Wintershall Holding (Germany) (Quadri and Shuaib, 1986; Fig. 1).

We employ a series of established weathering proxies based on clay mineralogy as well as bulk sediment geochemistry in order to define the state of alteration of the recovered sediment. We then use these data to examine how weathering in the onshore river basin changed through geologic time. We use a matrix of different proxies in order to establish confidence in the long-term weathering history, and we test to see whether changes in chemical weathering intensity are linked to tectonic or global climatic variation.

The alteration state of any particular sediment is controlled not only by the rate of chemical weathering but also by the duration over which it occurs (Wan et al., 2017) as well as the complexity of geomorphic and biological settings (Goudie and Viles, 2012). As a result, links between climate and chemical weathering are complicated. For example, wetter conditions may result in faster weathering rates, but the higher precipitation may also increase discharge in river systems and shorten transport times, providing less opportunity for fresh minerals to be degraded into chemical weathering products such as clays (Dosseto et al., 2008, 2015; Selvaraj and Chen, 2006).

We undertake this investigation in the Arabian Sea, where the sediment has been largely derived from the high mountains of the Himalaya, Karakoram, and adjacent ranges (Fig. 1). Although there is evidence that the patterns and sources of erosion have changed through time (Clift et al., 2008a; Zhuang et al., 2018), there is no indication that the drainage basin itself has changed radically in its extent since the late Miocene (Burbank et al., 1996; Clift et al., 2019b). We make use of existing provenance data from the studied boreholes to constrain the possible influence of changing sources in governing clay mineralogy and sediment chemistry (Clift et al., 2019b; Khim et al., 2019; Yu et al., 2019), and in so doing, we allow their relationships with regional climate and tectonic processes to be investigated.

We analyze sediments recovered by IODP Expedition 355, which recovered long sections of sediment in the Laxmi Basin of the eastern Arabian Sea, offshore western India (Pandey et al., 2016c). Drilling at IODP Site U1456 penetrated a ~1100-m-thick sequence of turbidite silts and sandstones, mudstones, and occasional carbonates before bottoming in a large mass-transport deposit emplaced at ca. 10.8 Ma (Fig. 2A) (Calvès et al., 2015). At Site U1457, drilling penetrated the mass-transport deposit, but the underlying sediment was dated as Paleocene, predating India-Asia collision and Indus Fan sedimentation (Fig. 2B) (Pandey et al., 2016b).

These sediments represent a variety of depositional settings in the deep-water basin, with the sandy material interpreted as turbidite lobe deposits on the upper fan, and the muddy material representing hemipelagic sedimentation that accumulated when the active lobes were located elsewhere in the basin so that distal fine-grained sedimentation via hypopycnal plumes dominated (Pandey et al., 2016c). A relative reduction in coarser siliciclastic sediment flux might represent times of reduced Indus River discharge, or a simple relocation of the fan depositional lobes out of the Laxmi Basin, or even a bloom in biogenic productivity offshore western India diluting the clastic flux. Nd isotope data from the fine-grained clastic sediments suggest that the vast majority were supplied from the Indus River (Clift et al., 2019b), with lesser quantities derived from western India, especially in the past ~4 m.y., commonly linked to times of lower sea level (Khim et al., 2019; Yu et al., 2019).

HISTORY OF THE ASIAN MONSOON

Scientific drilling offshore of Arabia has demonstrated that oceanic upwelling, driven by summer monsoon winds, intensified no later than ca. 8 Ma (Kroon et al., 1991; Prell et al., 1992). More recent analysis now indicates that the first strengthening may date from ca. 13 Ma (Gupta et al., 2015), consistent with new constraints on biogenic production in the Maldives, also linked to seasonal winds (Betzler et al., 2016). While marine biogenic production now correlates with the intensity of summer monsoon rains (Curry et al., 1992), it is not clear whether the same was always true in the deep geologic past (Clift, 2017). Other proxy records suggest that the monsoon may be somewhat older, and that the late Miocene was a time of drying (Clift et al., 2008b; Dettman et al., 2001). Carbon isotopes from the western Himalayan foreland basin measured from freshwater bivalve shells and teeth (Dettman et al., 2001) as well as pedogenic carbonates (Singh et al., 2011) indicate a transition from woody-dominated vegetation to a more grass-dominated assemblage after ca. 8 Ma, suggestive of the drying trend (Dettman et al., 2001; Singh et al., 2011). This interpretation is consistent with apparent reductions in erosion rates based on records from many Asian marginal seas at that time (Clift, 2006; Wu et al., 2019) as well as records of chemical weathering in the South China Sea (Clift et al., 2014; Wan et al., 2007). Since the onset of Northern Hemispheric glaciation (NHG) at ca. 2.7 Ma (Raymo, 1994; Zhang et al., 2009), the intensity of the South Asian monsoon has varied strongly with these glacial-interglacial cycles. In general, the summer rains are stronger when the global climate is warm and become weaker during phases of strong glaciation when colder, drier conditions tend to dominate in lower latitudes (Clemens and Prell, 2003, 2007).

In the present day, the Indus Basin is affected by summer monsoon rains but also receives moisture during the winter via the westerly jet, especially in the northern parts of the flood plains, close to the Himalayan front, as well as in the Karakoram in the form of snow (Demske et al., 2009; Karim and Veizer, 2002). Spring melting of this snow is an important part of the total discharge to the Indus River, in contrast to the eastern Ganges-Brahmaputra River basin (Immerzeel et al., 2010). In general, the Indus Basin lies on the edge of the Asian monsoon precipitation maximum and is thus more sensitive to changes in rainfall intensity compared to the eastern parts of the Himalaya (Bookhagen and Burbank, 2006). This makes the Indus especially suitable for looking at the impact of changing monsoon strength on the development of landscape and

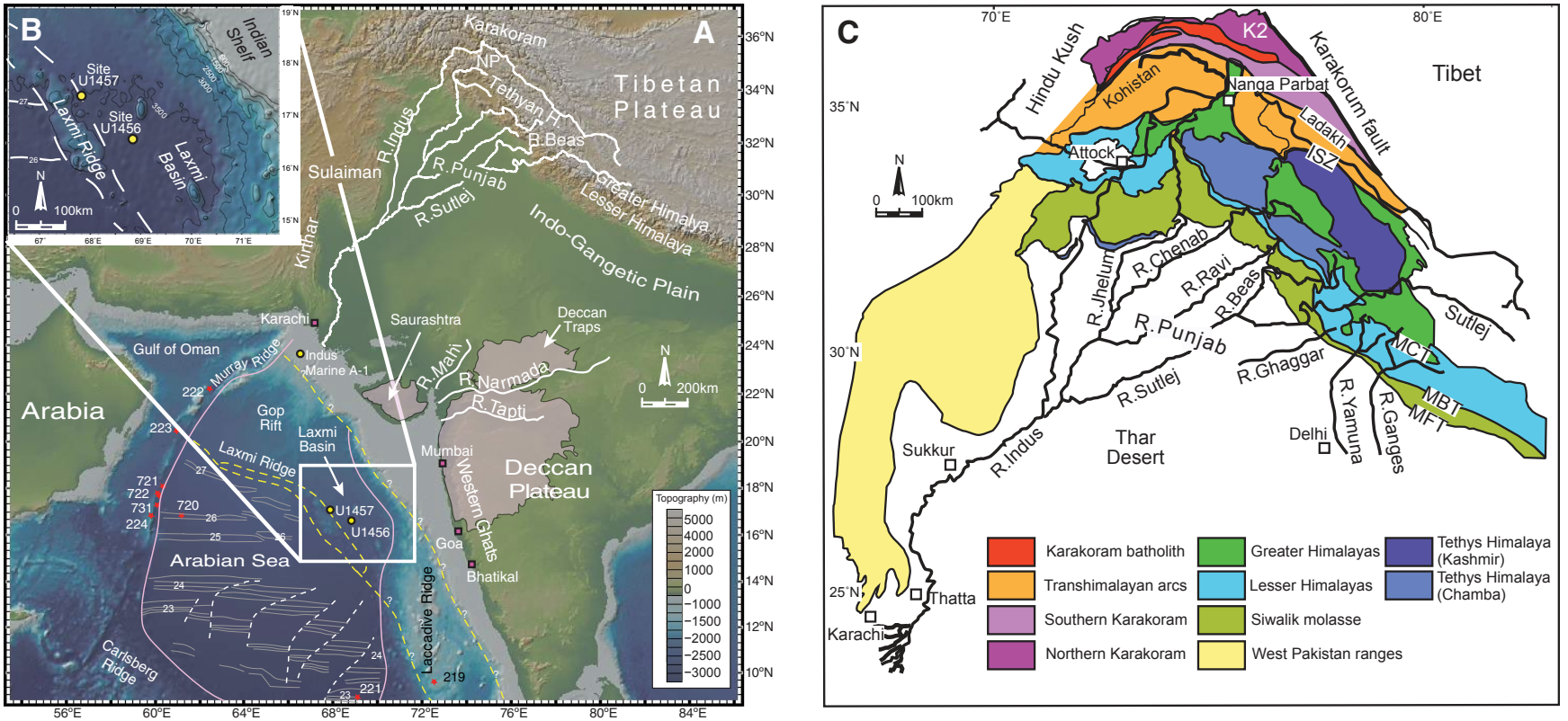

Figure 1. (A) Shaded bathymetric and topographic map of the Arabian Sea area showing the location of the drilling sites within the Laxmi Basin considered by this study (yellow circles). Map also shows the primary source terranes and the major tributary systems of the Indus River, as well as smaller peninsular India rivers that may have provided material to the drill sites. Numbered red circles indicate existing scientific boreholes from the Deep Sea Drilling Project (sites 219, 221, 222, 223, and 224) and the Ocean Drilling Program (sites 721, 722, and 731). Thin white lines and numbers are magnetic anomalies; lineation from Miles and Roest (1993). White dashed lines show transform faults. NP—Nanga Parbat. Base-map data is from GeoMapApp (http://www.geomapapp.org). (B) Inset map showing detail of the Laxmi Basin and location of the International Ocean Discovery Program drill sites considered in this study. Bathymetric contours are labeled in meters; contour interval is 500 m. (C) Geological map of the western Himalaya showing the major tectonic units that are eroded by the Indus River and its tributaries. Map is modified after Garzanti et al. (2005). Rivers are shown as thick black lines. ISZ—Indus suture zone; MCT—Main central Thrust; MBT—Main Boundary thrust; MFT—Main Frontal thrust. Thick black line shows the boundary of the Indus drainage, while thinner lines demark the limits of the major Himalayan tributaries.

chemical weathering. In particular, do stronger summer rains result in more erosion and stronger chemical weathering, or does faster sediment transport driven by higher discharge cause sediment to be less altered?

REGIONAL GEOLOGY

Indus Marine A-1 is a petroleum exploration well that penetrated 2831 m into mid-Miocene siliciclastic sediments in the middle of the Indus shelf, west of the Indus Canyon and ~75 km southwest of the modern river mouth (Shuaib, 1982). In this location, the post-rift sequences are generally flat lying and affected by mild growth faulting representing the gravitational collapse of the outer shelf. IODP Sites U1456 and U1457 are located in the Laxmi Basin, which forms the eastern part of the Arabian Sea (Fig. 1). The basin is separated from the main oceanic Arabian Basin by the continental Laxmi Ridge. The Laxmi Basin rifted during the latest Cretaceous when India began to separate from the Seychelles as seafloor spreading initiated between these continental fragments (Bhattacharya et al., 1994; Pandey et al., 1995). Following the onset

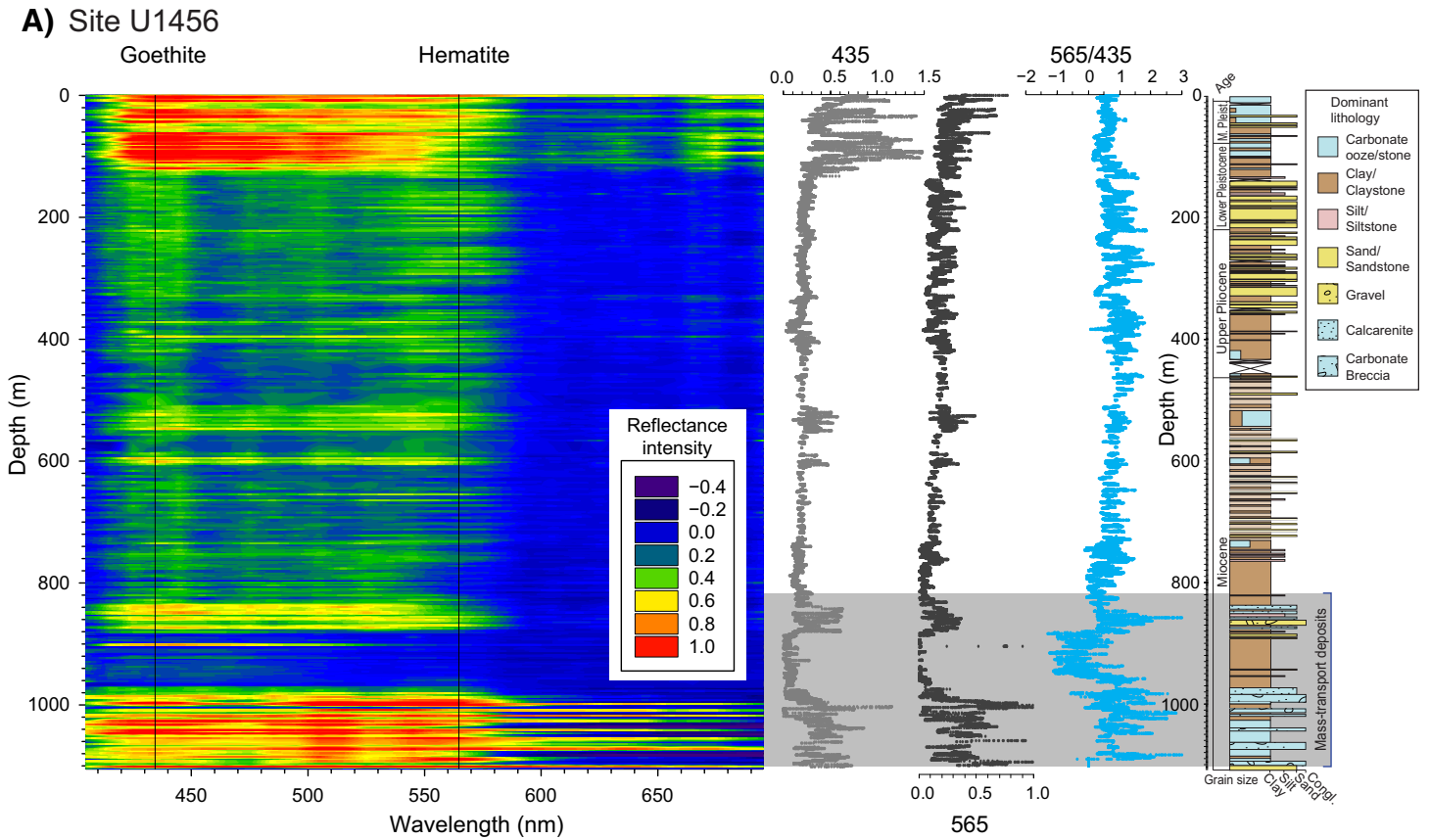

Figure 2. Plot of depth against wavelength for diffuse reflectance spectroscopy data. (A) International Ocean Discovery Program (IODP) Site U1456. The first-order derivatives of the reflectance intensity of 435 nm represent the relative abundance of goethite, and 565 nm represent the relative abundance of hematite. The 565/435 plot here represents the relative hematite/goethite ratio. Paleoc.—Paleocene; M.—Middle; U.—Upper; Pleist.—Pleistocene; Congl.—conglomerate. (*Continued on following page.*)

of India-Asia collision (ca. 50–60 Ma) (DeCelles et al., 2014; Ding et al., 2016; Najman et al., 2010), the uplift and erosion of the Himalaya drove faster bedrock erosion and supplied large sediment volumes to the submarine Indus Fan. The Indus Fan is the second largest sediment body on Earth after the Bengal Fan located between India, Bangladesh, and the Andaman Islands. The Indus Fan totals 4–5 × 10^6 km^3 (Naini and Kolla, 1982). The fan reaches a thickness of >11 km under the Indus shelf (Clift et al., 2001), but is much thinner in the Laxmi Basin (Kolla and Coumes, 1987; Nair and Pandey, 2018).

Sites U1456 and U1457 lie above the carbonate compensation depth, making it possible to date the age of sedimentation using a combination of nannofossil and foraminiferal biostratigraphy coupled with magnetostratigraphy that has produced the relatively robust age model by Routledge et al. (2019). Ages at Site U1456 were constrained by 41 age picks going back to 15.62 Ma, while 51 age picks constrained the depositional age at Site U1457, extending to 63.25 Ma. In general, the age resolution is highest in the youngest part of the section where age control points are separated by ~0.2–0.04 m.y., while in the Miocene section this increases from 0.14 to as much as 0.76 m.y. Sedimentation rates are assumed to be linear between control points.

Sediment at Site U1456 is generally coarser grained than at Site U1457 because the former site lies in the center of the Laxmi Basin, while the latter is positioned on the eastern flank of the Laxmi Ridge where it has received less siliciclastic sediment from turbidity currents, which tend to focus into the topographic low in the basin center (Pandey et al., 2016c). The primary source of sediment to these sites is the Indus River (Clift et al., 2019b), although the

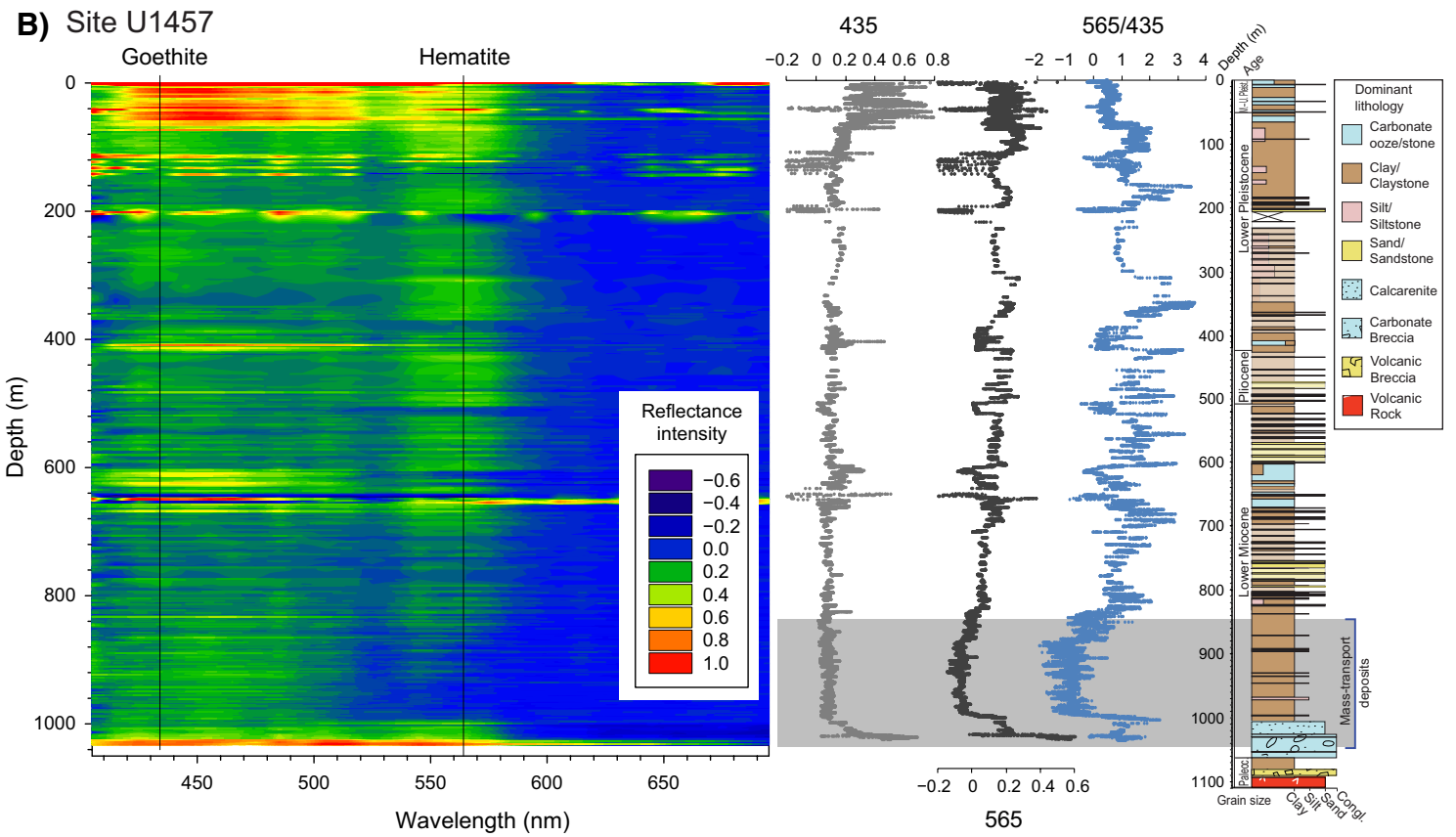

Figure 2 (*continued*). (B) IODP Site U1457.

sites also received lesser inputs of fine-grained sediment from rivers draining the Indian peninsula, including the Tapti, Mahi, and Narmada Rivers (Khim et al., 2019; Yu et al., 2019) (Fig. 1). Petrographic investigations indicate that there have been limited amounts of sediment delivery from western India, mostly in the youngest parts of the section (Andò et al., 2019), but that the heavy mineral assemblages are consistent with sources in the Himalaya, not the Indian peninsula. Bulk-sediment Nd isotope measurements (Yu et al., 2019) indicate a dominantly Indus-derived supply during interglacial times and more erosion from the Indian peninsula during glacial times when sea level was low. This type of variability affected the region only after the onset of NHG. A lower-resolution study of Nd isotopes and associated zircon U-Pb ages spanning the longer time interval considered here indicates that provenance within the basin was mostly stable and dominantly from the Indus (Clift et al., 2019b), consistent with fission-track data from the same sediments (Zhou et al., 2019).

Other sediment sources are not important inputs to the IODP sites studied here. Wind patterns do not now favor eolian transport from Arabia, although some supply from the Somali region might be possible at the present time based on regional wind patterns (Vecchi et al., 2004). Sediment trap data from the western and central Arabian Sea document reduced eolian sedimentation moving east away from Arabia (Pease et al., 1998). The highest eolian sedimentation rates occur during the winter and spring when the South Asian winter monsoon can transport material from the Thar Desert (northwestern India and southeastern Pakistan), which is itself derived from the Indus delta (East et al., 2015). Given they have the same or similar sources, it is difficult to resolve

eolian from water-transported sediment. Nonetheless, sedimentation rates suggest that eolian processes are not significant in comparison to the fluvial sources. In the upper Miocene at Site U1456, during one of the slower periods of accumulation, sedimentation rates were ~10 cm/k.y. Assuming an average dry sediment density of ~1.6 g/cm^3, this is equivalent to ~16 g/cm^2/k.y. of total siliciclastic sedimentation. In contrast, modern sediment traps offshore western India constrain average eolian sedimentation rates to 0.29–1.05 g/cm^2/k.y. (Honjo et al., 1999). This means that the eolian contribution was a very small fraction of the total deposit, even when fan sedimentation rates were slow.

The sediment supplied by the Indus is derived from a number of mountain ranges at the western end of the Himalaya and Tibetan Plateau. Study of modern sediment suggests that the Karakoram and Himalaya dominate the sediment supply to the Indus River (Clift et al., 2002; Garzanti et al., 2005) and that the balance between the two is dependent on monsoon strength, with supply being more Himalayan when the summer rains are strong (Clift et al., 2008a). The source regions have not always been as they are today because the foreland basin sedimentary rocks of the Siwalik Group (Fig. 1C) have been uplifted above the flood plains most recently (Lavé and Avouac, 2000). Even the Lesser Himalaya only started to contribute large volumes after ca. 3 Ma (Clift et al., 2019b), although evidence from the proximal foreland basin indicates that these were first exposed after ca. 9 Ma, at least locally (Huyghe et al., 2001; Najman et al., 2009). The Greater Himalaya, comprising high-grade metamorphic rocks and granites, are somewhat older and record their strongest cooling and exhumation in the early Miocene (Stephenson et al., 2001; Walker et al., 2001). In contrast, the Tethyan Himalaya that lie north of the Greater Himalaya and which represent the telescoped, but weakly metamorphosed, passive margin of Greater India (Garzanti et al., 1987) have been available for erosion since long before the start of our studied period (Webb, 2013). Sediment is also supplied from the terrains that represent the old active margin of Eurasia, most notably the Karakoram, as well as the accreted oceanic arc rocks of Kohistan and the along-strike, but less metamorphosed, sequences of the Hindu Kush (Zhuang et al., 2018).

Although there is evidence for sediment storage and reworking as material is transported to the Arabian Sea, the time scale of this process is generally 10^4–10^5 yr (Blöthe et al., 2014; Clift and Giosan, 2014; Jonell et al., 2017), so this should not be very important on the much longer time scales considered here. Greater reworking likely occurred when the foreland basin was partly eroded ca. 20 Ma (Najman, 2006), but again, this precedes the studied time interval so that the material analyzed here is largely the product of erosion close to the time of sedimentation. Much of the chemical weathering would have been achieved in the flood plains rather than in the mountains themselves or after deposition (Lupker et al., 2012). Bickle et al. (2018) estimated that the flood plains contribute 41%–63% of the major cation fluxes to the Ganges delta, compared to 24% from the Himalayan rivers, although Be isotope measurements from the Ganges flood plain imply short transport times and low degrees of weathering on the flood plain, at least in the modern day (Rahaman et al., 2017).

CHOICE OF PROXIES

In this study we use a range of chemical weathering proxies to constrain the alteration state of the sediment recovered from the IODP drill sites. This work extends the analysis of the 5.5–8.5 Ma period considered by Clift et al. (2019a), which was more limited in time duration, focused only on Site U1456, and relied on remotely scanned X-ray fluorescence data rather than the more conventional sample analysis chosen here. Geochemical proxies are based on the changing relative concentrations of elements readily mobilized during chemical weathering (e.g., Na, K, Ca, Mg) and aluminosilicate-bound Al and Si. We use the chemical index of alteration (CIA) proxy of Nesbitt et al. (1980) as being a well-defined alteration proxy with a correction made for excess Ca where appropriate, following the method of Singh et al. (2005). We use their CIA* in place of regular CIA value following this method. Fresh granitic bedrock has a CIA value close to 50, while fully weathered material has a value of ~100. A detailed analysis of chemical weathering data from the South China Sea suggested that Mg/Al is not reliable as a weathering proxy in that it shows little relationship to other proxies or climate records (Hu et al., 2016). However, our study did support use of K/Si and Na/Si as weathering intensity proxies. Si/Al is used as an associated grain-size proxy, based on the concept that Si is rich in sediment dominated by quartz silt and sand while Al is more common in clay-rich sediments.

Illite and chlorite are formed during diagenesis and low-grade metamorphism and are generally associated with physical erosion of bedrock containing these minerals. In contrast, kaolinite and smectite are products of chemical weathering. Kaolinite is mostly associated with intense leaching under tropical conditions (Thiry, 2000), while smectite is commonly linked to the breakdown of volcanic bedrock sources (Hillier, 1995). The kaolinite/smectite value can be used as a measure of how tropical, rather than seasonal, the weathering environment might have been (Alizai et al., 2012). However, analysis of the modern and Holocene Indus flood plains shows that ~40%–50% of the clay minerals is smectite (Alizai et al., 2012). Ratios of smectite or kaolinite compared to illite and/or chlorite have a long history of being used to determine chemical weathering intensities, including in several examples from monsoonal Asia (Colin et al., 1999; Liu et al., 2019; Liu et al., 2005). Alteration can also be charted using illite crystallinity (Gingele et al., 2001, 1998). Illite crystallinity, calculated from the full width at half maximum height (FWHM) of the X-ray diffraction (XRD) illite 10 Å peak, is also used here as an index of chemical weathering (Chamley, 1989), and is interpreted to reflect the hydrolyzing power of the soil from which the mineral was derived (Lamy et al., 1998). Higher temperatures and more rainfall lead to stronger hydrolyzation, more chemical weathering, wider XRD peaks, and higher values of illite crystallinity. As a result, illite crystallinity can be a good proxy for assessing whether monsoon intensity affects chemical weathering.

We track evolving humidity and temperature using a spectrally derived estimate of the hematite/goethite ratio. Hematite usually represents dry, warmer environments (Schwertmann, 1971), while goethite is generally associated with

cooler, wetter environments (Sangode and Bloemendal, 2004; Schwertmann, 1971). This ratio has previously been used as a proxy of relative humidity (Balsam et al., 1997; Giosan et al., 2002b; Ji et al., 2002) but may be subject to change during diagenesis. Iron-oxide reduction, which can affect the measured ratio, is typically limited to the upper meter of the sediment column (Canfield et al., 1992) and would not be significant on the scale we consider here, i.e., several hundred meters. Pore-water chemistry from both drill sites does not indicate anomalous shallow diagenesis, and in general, rapidly deposited Fe-rich sediments with modest organic carbon contents generally retain some of the original iron oxides through this reduction zone (Roberts, 2015). Rock magnetic studies of sediments from the Bengal Fan have highlighted the possible role of organic carbon in controlling pyrite formation and the degree of deeper diagenesis, which in turn influence the hematite and goethite abundances. However, it should be recognized that the Bengal Fan is consistently more efficient in organic carbon burial compared to the Indus (Galy et al., 2007). Clift et al. (2019a) plotted total organic carbon against the ratio of the first-order derivatives of the 565 nm and 435 nm wavelengths, which represent the relative abundance of hematite compared to goethite at IODP Site U1456 and noted a lack of any coherent variation. This implies that the patterns displayed here are not heavily influenced by burial. The hematite/goethite record provides an important additional method to help resolve the effect of climatic change. Lower hematite/goethite values would indicate more rainfall, potentially linked to summer monsoon intensification, although a strong seasonality involving a dry season as well could promote higher hematite/goethite values.

We further track chemical weathering using magnetic susceptibility (MS). MS is linked to the mineralogy of the Fe-bearing minerals in the sediment and, as such, is controlled by environmental conditions during chemical weathering in flood plains as well as diagenesis. The concentrations of magnetite and hematite as well as Fe-sulfides like pyrrhotite and greigite are the primary controls over sediment magnetic susceptibility (Dekkers, 1978). Reduction of iron during burial occurs in the shallow subsurface (Coleman et al., 1993) so that over longer sections, variations in MS are considered to reflect significant variations in the original sediment composition that may be related to change in sediment type and provenance. Depositional setting can also be important in controlling the magnetic mineralogy, but all the sediments considered here were deposited in a deep-water basin. MS has been applied for paleoenvironmental studies in sedimentary sections, such as the Chinese Loess Plateau, where strongly weathered soils rich in Fe-bearing minerals have high MS and contrast with low-MS loess sediment deposited during drier intervals (An et al., 1991; Heller and Evans, 1995).

METHODS

One-hundred fifteen (115) samples from IODP Sites U1456 and U1457 and the Indus Marine A-1 borehole were selected for bulk sediment major element geochemical analysis, which was conducted by inductively coupled plasma emission spectrometry (ICP-ES) at Boston University (BU; Boston, Massachusetts, USA). Sediment samples were decarbonated with 20% acetic acid for at least two days until no further bubbles were noted, then washed with distilled and deionized water with a purity of 9–12 MΩ and hand powdered at Louisiana State University (LSU; Baton Rouge, Louisiana, USA) before total fusion preparation at BU. Glass beads for each sample were made in a muffle furnace at 1050 °C by fusing 100 ± 0.5 mg of sample mixed with 400 ± 0.5 mg lithium metaborate ($LiBO_2$). We did not undertake a loss on ignition (LOI) measurement because the organic carbon contents are generally low in these sites, ~0.5% (Pandey et al., 2016a, 2016b). LOIs can be problematic in the analysis of marine sediments because if samples have high $CaCO_3$ or organic carbon, then the result after LOI is by definition on a volatile-free basis and not the original compositional mass. In the case of samples with low $CaCO_3$ or organic carbon, measuring LOI also drives off not just the pore water but also much of the mineralogically bound water, which in the case of clays can be 10%–20% of the sediment by mass; this results in an analytical outcome that is not based on the mass of the total original sample. The melted mixture was then dissolved in 50 ml 5% HNO_3, sonicated, manually shaken (not stirred) until no visible grains were observed, and further diluted for analysis following the methods of Dunlea et al. (2015). We analyzed the international standard reference material BHVO-2 (basalt, Hawaiian Volcano Observatory, U.S. Geological Survey) (Wilson, 1997) with three separate fusions. In terms of accuracy (the percent difference relative to literature values), the major elements were all in the range of 0.2% (SiO_2) to 3.7% (K_2O). All elements except K_2O and MnO showed <2% uncertainty. In the case of the trace elements, accuracy for Sr was 0.1%, for Ba was 2.75%, and for Zr was 5.31%. Analytical results are provided in Table 1. Nine of the samples from Indus Marine A-1 showed elevated Ba concentrations (>1500 ppm), and although they showed similar major element compositions, four of these were more variable and fell outside the range of the other samples. We do not plot these questionable data in the figures.

Clay mineralogy measurements were undertaken at LSU using a Panalytical Empyrean X-ray diffractometer. The samples are mostly the same as those selected for bulk geochemical analysis; in some cases, all the sample material taken for geochemistry was used up for that purpose and clay mineralogy had to be conducted on adjacent samples. These samples were decarbonated with 20% acetic acid and then soaked in distilled water until there was no flocculation, with Na_3PO_4 added to de-flocculate when necessary. Four XRD patterns were generated from each oriented sample smear. The first was collected from the sample in the air-dried condition. The slide was then placed in a desiccator with ethylene glycol for a minimum of eight hours at 25 °C, and the second XRD pattern was generated from the glycolated sample. The third and fourth XRD data sets were collected after the sample was subjected to heat treatments of 300 °C for one hour, and then 550 °C for another hour, respectively. XRD analysis began immediately after glycolation and immediately after the first heat treatment. The semiquantitative method of Biscaye (1965) was used to estimate the clay assemblage, which is based on peak-intensity factors determined from calculated XRD patterns, as measured by MacDiff software (http://www.geol-pal.uni-frankfurt.de/Staff

TABLE 1. MAJOR ELEMENT COMPOSITION OF SEDIMENTS DERIVED BY INDUCTIVELY COUPLED PLASMA–EMISSION SPECTROSCOPY

Sample name	Depth below top of core section (cm)	Age (Ma)	SiO_2 (wt%)	Al_2O_3 (wt%)	Fe_2O_3 (wt%)	MgO (wt%)	TiO_2 (wt%)	CaO (wt%)	Na_2O (wt%)	K_2O (wt%)	P_2O_5 (wt%)	MnO (wt%)	Sr (ppm)	Ni (ppm)	Ba (ppm)	V (ppm)	Zr (ppm)	Sc (ppm)	Y (ppm)	Total (wt%)	ε_{Nd}
U1456A-6H-5	145–150	0.476	72.5	12.5	3.7	1.7	0.6	1.5	2.3	2.3	0.0	0.0	163	N/A	405	N/A	195	N/A	N/A	97.2	–13.46
U1456A-25F-3	75–80	1.308	61.4	16.3	6.1	2.8	0.8	1.4	1.8	3.2	0.1	0.1	161	N/A	504	N/A	147	N/A	N/A	94.1	–11.96
U1456A-26F-3	50–58	1.317	71.1	12.2	3.8	1.5	0.6	1.5	2.0	2.5	0.1	0.0	N/A	N/A	345	N/A	215	141	N/A	95.3	N/A
U1456A-58F-1	89–99	1.631	52.8	15.1	8.2	4.8	0.9	0.9	0.9	2.8	0.2	0.1	106	216	534	198	184	20	38	86.8	–8.68
U1456A-63F-1	140–150	2.494	57.9	17.9	6.2	2.8	0.8	0.6	1.1	3.5	0.1	0.0	101	N/A	642	N/A	177	N/A	N/A	91.2	–12.76
U1456A-63F-2	20–30	2.499	68.3	13.1	4.6	2.0	0.7	1.5	1.9	2.5	0.1	0.0	N/A	N/A	462	N/A	230	137	N/A	94.9	N/A
U1456A-70F-2	10–16	3.017	60.9	16.2	5.9	2.7	0.8	1.1	1.4	3.2	0.1	0.0	N/A	N/A	492	N/A	169	131	N/A	92.4	N/A
U1456A-72X-4	140–150	3.290	49.3	15.6	8.9	4.1	1.1	1.1	0.5	2.8	0.2	0.1	114	125	580	162	173	23	31	83.8	–9.30
U1456C-45X-2	111–121	3.565	59.7	16.7	6.5	2.7	0.8	0.6	1.1	3.1	0.1	0.0	106	N/A	500	N/A	202	N/A	N/A	91.6	–11.92
U1456C-45X-3	45–51	3.567	64.8	14.3	5.2	2.4	0.7	1.1	1.6	2.9	0.1	0.0	N/A	N/A	424	N/A	139	132	N/A	93.3	N/A
U1456D-3R-CC	10–15	5.564	59.6	17.7	6.4	2.8	0.9	0.5	1.1	3.3	0.1	0.0	108	N/A	486	N/A	186	N/A	N/A	92.6	–11.45
U1456D-5R-1	12–20	5.720	61.9	15.4	5.7	2.6	0.8	1.1	1.5	3.0	0.1	0.0	N/A	N/A	474	N/A	220	132	N/A	92.3	N/A
U1456D-5R-2	94–104	5.736	68.3	13.6	4.9	2.0	0.7	1.4	1.9	2.6	0.1	0.0	171	N/A	484	N/A	213	13	26	95.6	N/A
U1456D-6R-CC	5–10	5.793	57.1	16.8	7.2	3.0	0.9	0.8	0.8	3.1	0.2	0.1	110	81	432	139	203	17	27	90.1	–11.53
U1456D-7R-1	84–94	5.869	63.2	14.5	5.5	2.3	0.8	1.2	1.6	2.7	0.1	0.0	147	N/A	484	N/A	205	14	27	92.0	N/A
U1456D-8R-5	140–150	6.152	58.9	14.8	6.3	3.4	0.8	1.0	1.1	2.5	0.1	0.0	125	N/A	429	N/A	181	12	17	89.2	N/A
U1456D-9R-5	123–133	6.538	54.6	15.8	7.6	4.4	0.9	0.6	0.8	2.9	0.1	0.1	95	N/A	495	N/A	172	20	22	87.9	N/A
U1456D-10R-3	135–145	6.790	54.0	15.8	7.4	4.1	0.9	0.4	0.7	2.8	0.1	0.1	78	N/A	407	N/A	160	N/A	N/A	86.3	–7.69
U1456D-14R-CC	10–15	7.132	58.1	15.9	6.7	3.1	0.8	0.9	1.0	3.0	0.1	0.0	118	82	318	126	179	17	24	89.7	–10.34
U1456D-17R-CC	10–15	7.552	57.8	16.7	5.3	2.7	0.8	0.6	1.2	3.1	0.1	0.0	113	N/A	348	N/A	167	N/A	N/A	88.3	–9.36
U1456D-20R-1	95–103	7.719	63.5	14.5	4.9	2.4	0.7	1.4	1.6	2.8	0.2	0.0	N/A	N/A	305	N/A	191	145	N/A	92.1	N/A
U1456D-22R-1	73–83	7.837	62.4	15.5	5.4	2.6	0.8	1.3	1.6	2.9	0.1	0.0	N/A	N/A	338	N/A	170	146	N/A	92.8	N/A
U1456D-27R-2	100–106	8.149	62.6	15.1	5.4	2.7	0.8	1.2	1.4	2.8	0.2	0.0	N/A	N/A	326	N/A	162	136	N/A	92.4	N/A
U1456D-28R-1	40–46	8.196	62.6	14.9	5.3	2.6	0.7	1.2	1.6	2.7	0.2	0.0	N/A	N/A	363	N/A	188	141	N/A	91.9	N/A
U1456D-29R-2	24–34	8.266	62.1	15.3	5.4	2.7	0.8	1.1	1.5	2.8	0.1	0.0	N/A	N/A	352	N/A	181	133	N/A	91.9	N/A
U1456D-29R-2	128–143	8.269	58.1	17.1	5.8	3.0	0.8	0.8	1.0	3.0	0.1	0.0	115	N/A	329	N/A	161	N/A	N/A	89.7	–10.26
U1456D-30R-CC	0–5	9.268	51.6	16.9	9.0	3.1	1.3	0.2	0.4	2.6	0.1	0.0	60	N/A	413	N/A	170	N/A	N/A	85.3	–7.14
U1456D-35R-4	107–122	9.759	48.7	15.8	9.0	3.8	1.0	0.3	0.1	2.9	0.2	0.1	120	139	404	153	162	23	25	81.9	–8.82
U1456D-38R-1	22–24	9.872	53.0	17.1	7.9	3.3	1.1	0.2	0.4	3.0	0.1	0.0	96	N/A	431	N/A	152	N/A	N/A	86.3	–8.17
U1456D-42R-6	40–42	10.422	53.4	16.2	8.6	4.1	1.0	0.2	0.7	3.3	0.1	0.1	83	N/A	369	N/A	162	N/A	N/A	87.7	–7.90
U1456D-46R-4	8–10	10.601	53.6	16.8	8.3	3.2	1.4	0.3	0.6	2.9	0.1	0.0	90	N/A	404	N/A	199	N/A	N/A	87.3	–8.35
U1456D-49R-1	50–52	10.670	49.6	17.2	9.5	3.0	1.5	0.5	0.4	2.7	0.1	0.1	125	N/A	414	N/A	179	N/A	N/A	84.7	–8.54
U1456D-52R-5	65–67	10.768	56.3	15.8	6.8	4.1	1.0	0.2	0.8	3.2	0.1	0.0	81	N/A	350	N/A	205	N/A	N/A	88.4	–8.72
U1456D-52R-5	80–88	10.770	51.1	17.2	8.5	3.3	1.2	0.3	0.4	3.2	0.1	0.0	N/A	N/A	309	N/A	147	102	N/A	85.3	N/A
U1456D-54R-1	5–7	10.806	53.2	17.1	8.3	3.2	1.3	0.2	0.5	3.1	0.1	0.0	90	N/A	367	N/A	167	N/A	N/A	87.1	–9.77
U1456D-59R-5	10–12	11.534	54.8	11.5	7.5	3.2	0.7	1.3	0.6	2.3	0.1	0.0	738	N/A	2088	N/A	172	N/A	N/A	82.3	–1.52
U1456D-60R-1	109–111	11.691	53.1	11.4	7.0	3.4	0.7	1.5	0.4	2.0	0.3	0.1	308	N/A	1806	N/A	82	N/A	N/A	80.0	N/A
U1456E-12R-1	112–114	13.233	51.5	12.9	8.8	3.3	0.9	1.3	0.3	1.8	0.1	0.0	109	N/A	736	N/A	182	N/A	N/A	80.9	–7.55
U1456E-17R-7	42–44	15.065	49.5	14.6	9.6	3.3	1.1	1.2	0.2	2.2	0.1	0.1	109	N/A	1251	N/A	160	N/A	N/A	81.8	–8.86
U1456E-19R-3	10–20	15.566	65.1	13.9	5.0	2.7	0.7	1.1	1.7	2.7	0.1	0.0	N/A	N/A	316	N/A	182	142	N/A	93.2	N/A
U1456E-19R-CC	17–22	15.628	70.8	12.4	3.6	2.0	0.5	1.5	2.2	2.3	0.1	0.0	180	N/A	357	N/A	163	N/A	N/A	95.6	–8.68
U1457A-1H-2	83–87	0.024	61.6	14.2	5.8	2.9	0.8	1.4	1.7	2.6	0.2	0.0	153	N/A	710	N/A	200	N/A	N/A	91.5	–10.53
U1457A-7H-5	135–137	1.026	50.5	14.3	8.0	3.4	1.1	1.3	0.8	2.3	0.1	0.0	171	N/A	483	N/A	148	N/A	N/A	81.9	–7.69
U1457C-24R-1	87–89	2.298	51.8	14.4	8.2	3.1	1.6	1.5	1.2	1.9	0.1	0.0	125	N/A	582	N/A	181	N/A	N/A	83.8	–7.20
U1457C-31R-1	94–100	3.169	62.2	15.6	5.7	2.6	0.7	1.2	1.9	3.7	0.2	0.1	N/A	N/A	541	N/A	177	152	N/A	93.9	N/A
U1457C-31R-2	72–74	3.185	64.6	15.5	5.1	2.5	0.8	1.3	1.9	3.1	0.1	0.0	162	N/A	527	N/A	175	N/A	N/A	95.2	–11.33
U1457C-33R-3	10–17	3.393	66.9	13.6	4.7	2.3	0.7	1.4	1.9	2.7	0.1	0.0	N/A	N/A	410	N/A	142	147	N/A	94.5	N/A

(*continued*)

TABLE 1. MAJOR ELEMENT COMPOSITION OF SEDIMENTS DERIVED BY INDUCTIVELY COUPLED PLASMA–EMISSION SPECTROSCOPY (*continued*)

Sample name	Depth below top of core section (cm)	Age (Ma)	SiO_2 (wt%)	Al_2O_3 (wt%)	Fe_2O_3 (wt%)	MgO (wt%)	TiO_2 (wt%)	CaO (wt%)	Na_2O (wt%)	K_2O (wt%)	P_2O_5 (wt%)	MnO (wt%)	Sr (ppm)	Ni (ppm)	Ba (ppm)	V (ppm)	Zr (ppm)	Sc (ppm)	Y (ppm)	Total (wt%)	ε_{Nd}
U1457C-35R-2	133–135	3.601	48.1	16.9	9.1	3.1	1.4	0.5	0.3	2.4	0.1	0.0	71	N/A	436	N/A	161	N/A	N/A	82.0	–8.06
U1457C-38R-1	2–4	5.621	49.7	17.3	9.1	3.3	1.3	0.6	0.5	2.6	0.1	0.0	88	N/A	447	N/A	143	21	18	84.6	N/A
U1457C-41R-1	0–2	5.765	61.8	15.3	5.7	2.4	0.8	1.1	1.3	2.8	0.1	0.0	141	N/A	415	N/A	178	11	22	91.5	N/A
U1457C-41R-2	20–26	5.773	64.9	14.7	5.3	2.4	0.8	1.2	1.6	2.7	0.1	0.0	N/A	N/A	414	N/A	210	135	N/A	93.8	N/A
U1457C-43R-2	52–60	5.871	65.6	14.2	5.0	2.3	0.7	1.3	1.7	2.9	0.1	0.0	N/A	N/A	395	N/A	194	141	N/A	94.0	N/A
U1457C-44R-1	16–20	5.910	60.2	16.1	6.2	2.7	0.8	0.9	1.3	2.9	0.1	0.0	128	N/A	491	N/A	172	16	26	91.3	N/A
U1457C-45R-6	92–94	6.741	54.4	16.7	7.3	3.7	1.0	0.8	0.9	3.3	0.1	0.0	112	N/A	535	N/A	152	N/A	N/A	88.4	–8.51
U1457C-46R-1	73–75	6.812	54.2	16.0	8.1	3.7	1.0	0.9	0.9	3.0	0.2	0.0	121	N/A	580	N/A	190	23	33	88.3	N/A
U1457C-46R-3	85–87	6.885	50.4	17.5	7.8	3.4	1.0	0.9	0.7	3.1	0.1	0.0	125	N/A	598	N/A	121	17	18	85.1	N/A
U1457C-47R-1	6–10	7.076	50.2	15.6	8.5	3.7	1.2	1.2	0.6	2.4	0.3	0.0	126	N/A	622	N/A	159	21	27	83.7	N/A
U1457C-49R-4	132–134	7.626	58.3	17.4	6.2	3.0	0.9	0.6	0.9	2.9	0.1	0.0	108	N/A	389	N/A	168	N/A	N/A	90.2	–9.85
U1457C-51R-4	80–88	7.772	66.1	13.9	4.8	2.3	0.7	1.4	1.8	2.7	0.1	0.0	N/A	N/A	311	N/A	154	154	N/A	93.9	N/A
U1457C-68R-4	130–134	8.666	58.4	14.5	6.7	2.7	1.0	0.9	0.9	2.6	0.2	0.0	108	N/A	356	N/A	211	16	23	87.9	N/A
U1457C-68R-CC	6–8	8.680	52.5	16.3	9.4	3.9	1.1	0.7	0.7	3.0	0.1	0.2	101	134	384	162	157	23	26	88.0	N/A
U1457C-68R-7	128–130	8.779	56.6	16.5	7.2	3.4	1.0	0.2	0.7	2.9	0.1	0.0	82	N/A	409	N/A	169	N/A	N/A	88.8	–9.15
U1457C-69R-1	100–104	8.779	58.4	15.4	7.1	2.9	1.1	0.5	0.9	2.8	0.1	0.0	91	N/A	384	N/A	195	N/A	N/A	89.4	–8.80
U1457C-69R-4	104–108	8.975	53.5	15.5	7.6	4.9	0.9	1.3	0.6	2.8	0.2	0.2	101	153	347	143	177	19	27	87.6	N/A
U1457C-69R-7	112–114	9.163	51.6	16.0	8.6	3.5	1.0	0.6	0.5	3.1	0.1	0.1	104	96	385	150	162	22	25	85.3	N/A
U1457C-70R-1	6–8	9.231	54.4	17.3	8.0	3.2	1.2	0.4	0.6	3.2	0.1	0.0	85	N/A	417	N/A	154	N/A	N/A	88.5	N/A
U1457C-70R-2	12–16	9.297	53.5	16.1	7.4	4.1	0.9	0.4	0.6	3.1	0.1	0.1	88	N/A	357	N/A	154	16	21	86.3	N/A
U1457C-70R-3	131–133	9.455	50.5	16.0	8.9	3.4	1.1	0.4	0.4	2.5	0.1	0.0	80	N/A	398	N/A	156	24	23	83.7	N/A
U1457C-73R-1	10–12	9.589	53.5	17.4	8.2	3.3	1.1	0.1	0.4	3.4	0.1	0.0	70	N/A	358	N/A	156	N/A	N/A	87.6	N/A
U1457C-70R-5	95–97	9.612	55.8	15.3	7.5	4.4	0.9	0.2	0.7	2.9	0.2	0.1	72	N/A	348	N/A	170	N/A	N/A	88.0	–6.50
U1457C-71R-1	7–9	9.704	52.5	17.4	8.3	3.4	1.2	0.3	0.4	3.1	0.1	0.0	73	N/A	338	N/A	143	N/A	N/A	86.7	N/A
U1457C-74R-2	19–21	9.939	62.7	14.1	5.7	2.8	1.0	0.5	1.0	2.7	0.1	0.0	94	N/A	370	N/A	216	N/A	N/A	90.7	–10.12
U1457C-76R-1	90–92	10.122	58.2	16.6	7.0	3.1	1.0	0.4	0.6	3.0	0.1	0.0	83	N/A	333	N/A	183	N/A	N/A	90.3	N/A
U1457C-77R-2	3–5	10.228	54.0	17.0	8.0	3.3	1.2	0.3	0.4	2.9	0.1	0.0	78	N/A	360	N/A	172	N/A	N/A	87.4	N/A
U1457C-78R-5	120-122	10.322	56.6	15.5	6.3	3.1	1.0	0.3	0.7	2.9	0.1	0.0	81	N/A	325	N/A	182	N/A	N/A	86.6	–10.71
U1457C-79R-5	120-122	10.432	58.4	16.0	7.1	3.2	1.0	0.4	0.7	3.1	0.1	0.0	81	N/A	299	N/A	216	N/A	N/A	90.1	N/A
U1457C-81R-1	30–32	10.545	57.5	15.9	6.7	3.0	1.0	0.3	0.6	2.9	0.1	0.0	76	N/A	273	N/A	181	N/A	N/A	88.2	–9.15
U1457C-81R-1	42–44	10.547	57.3	16.3	7.2	3.3	1.0	0.4	0.6	3.2	0.2	0.1	81	N/A	279	N/A	177	N/A	N/A	89.5	N/A
U1457C-82R-3	89–91	10.667	62.5	14.5	6.4	3.0	1.0	0.6	1.0	2.9	0.2	0.0	95	N/A	307	N/A	222	N/A	N/A	92.1	N/A
U1457C-83R-1	61–63	10.726	52.1	17.5	8.0	3.1	1.2	0.2	0.4	3.1	0.1	0.0	68	N/A	282	N/A	169	N/A	N/A	85.7	–9.95
U1457C-83R-2	18–20	10.735	51.5	16.8	9.2	3.5	1.1	0.3	0.4	3.1	0.1	0.1	113	109	251	171	171	26	27	86.3	N/A
U1457C-84R-6	101–103	10.853	56.8	15.8	7.1	3.9	0.9	0.3	0.7	3.3	0.1	0.1	78	N/A	267	N/A	185	N/A	N/A	89.0	N/A
U1457C-85R-1	60–62	10.913	57.9	16.0	7.1	4.0	0.9	0.3	0.7	3.4	0.1	0.0	83	N/A	274	N/A	185	N/A	N/A	90.5	N/A
U1457C-85R-3	46–50	10.925	53.6	15.3	7.9	4.6	0.9	1.0	0.7	3.2	0.2	0.2	116	189	261	147	185	21	34	87.6	N/A
U1457C-86R-1	6–8	10.983	54.4	15.5	8.0	4.4	0.9	0.8	0.8	3.3	0.2	0.1	117	173	267	147	174	20	33	88.3	N/A
U1457C-89R-3	119–121	11.195	52.3	13.0	7.5	4.0	0.8	0.9	0.4	2.4	0.1	0.0	82	N/A	309	N/A	139	N/A	N/A	81.5	–8.58
U1457C-94R-2	55–59	11.597	44.3	12.1	8.2	4.2	1.4	1.3	1.1	0.5	0.4	0.1	141	40	2	129	236	25	89	73.6	0.33
U1457C-95R-1	12–14	11.666	50.7	12.2	9.5	3.5	0.7	0.6	1.4	2.6	0.1	0.1	316	140	100	182	1128	22	90	81.5	N/A
U1457C-96R-1	62–66	11.756	50.5	12.6	10.3	3.2	1.0	0.4	0.0	2.1	0.0	0.4	57	N/A	100	N/A	134	N/A	N/A	80.5	–5.66
Indus Marine A-1-1620	N/A	3.597	60.3	15.3	7.9	2.8	0.8	1.1	1.5	3.1	0.1	0.1	357	N/A	4985	N/A	180	N/A	N/A	93.5	–10.38
Indus Marine A-1-2200	N/A	5.163	58.3	14.3	9.1	2.2	0.7	1.8	1.4	2.6	0.1	0.1	200	N/A	1512	N/A	210	N/A	N/A	90.8	–9.62
Indus Marine A-1-3180	N/A	6.926	56.5	14.6	6.9	2.4	0.8	1.1	1.3	2.7	0.1	0.0	1034	N/A	31,298	N/A	192	N/A	N/A	89.7	–9.89
Indus Marine A-1-3960	N/A	8.290	59.0	14.5	8.0	2.3	0.8	1.4	1.9	2.8	0.2	0.1	169	N/A	717	N/A	218	N/A	N/A	91.0	–10.03
Indus Marine A-1-4840	N/A	9.830	57.2	15.2	6.4	2.4	0.7	0.7	1.5	2.8	0.1	0.0	141	N/A	686	N/A	173	N/A	N/A	87.3	–10.73

(*continued*)

TABLE 1. MAJOR ELEMENT COMPOSITION OF SEDIMENTS DERIVED BY INDUCTIVELY COUPLED PLASMA–EMISSION SPECTROSCOPY (*continued*)

Sample name	Depth below top of core section (cm)	Age (Ma)	SiO_2 (wt%)	Al_2O_3 (wt%)	Fe_2O_3 (wt%)	MgO (wt%)	TiO_2 (wt%)	CaO (wt%)	Na_2O (wt%)	K_2O (wt%)	P_2O_5 (wt%)	MnO (wt%)	Sr (ppm)	Ni (ppm)	Ba (ppm)	V (ppm)	Zr (ppm)	Sc (ppm)	Y (ppm)	Total (wt%)	ε_{Nd}
Indus Marine A-1-4940	N/A	10.005	60.7	15.2	6.5	2.6	0.8	0.9	1.6	2.9	0.2	0.0	427	54	7977	119	223	14	23	92.2	–9.97
Indus Marine A-1-5360	N/A	10.716	57.3	15.6	7.8	2.8	0.8	0.7	1.5	2.7	0.2	0.1	138	N/A	743	N/A	190	N/A	N/A	89.5	–9.62
Indus Marine A-1-5920	N/A	11.665	59.3	17.3	7.6	2.9	0.9	0.3	1.4	3.1	0.1	0.0	124	N/A	573	N/A	181	N/A	N/A	92.9	–9.89
Indus Marine A-1-6360	N/A	12.355	57.2	16.8	7.2	3.1	0.9	0.7	1.2	3.1	0.2	0.0	126	75	535	133	191	16	24	90.3	–10.79
Indus Marine A-1-6460	N/A	12.512	60.6	16.0	6.7	2.7	0.8	0.4	1.4	2.8	0.1	0.0	121	N/A	497	N/A	229	N/A	N/A	91.6	–9.38
Indus Marine A-1-6890	N/A	13.186	59.0	16.9	7.0	3.1	0.9	0.8	1.1	3.0	0.2	0.0	140	83	489	140	192	15	25	92.2	–9.85
Indus Marine A-1-7090	N/A	13.499	61.1	16.8	7.1	3.0	0.9	0.2	1.1	3.0	0.1	0.0	103	N/A	467	N/A	208	N/A	N/A	93.3	–10.18
Indus Marine A-1-7190	N/A	13.656	59.5	15.4	8.1	2.9	0.8	0.7	0.9	2.7	0.2	0.1	127	105	764	130	223	14	24	91.3	–9.87
Indus Marine A-1-7400	N/A	13.985	58.1	16.1	7.8	3.1	0.8	0.6	0.9	3.1	0.1	0.0	122	102	521	131	198	16	24	90.9	–10.81
Indus Marine A-1-7500	N/A	14.142	59.1	16.2	7.6	3.1	0.9	0.6	0.7	3.0	0.2	0.0	127	114	518	139	225	16	24	91.4	–11.14
Indus Marine A-1-7620	N/A	14.330	58.5	16.1	7.2	3.1	0.9	0.6	0.8	3.0	0.2	0.0	109	91	484	126	225	16	25	90.4	–10.59
Indus Marine A-1-7720	N/A	14.487	59.0	16.5	6.5	3.0	0.9	0.3	1.1	3.0	0.1	0.0	104	N/A	463	N/A	191	N/A	N/A	90.5	–11.10
Indus Marine A-1-7820	N/A	14.644	57.8	16.1	7.0	3.1	0.9	0.6	0.9	2.9	0.1	0.0	114	88	530	127	216	15	23	89.5	–10.42
Indus Marine A-1-8040	N/A	14.989	58.4	16.3	7.1	3.1	0.9	0.6	0.8	3.1	0.1	0.0	110	105	466	132	206	15	25	90.7	–10.51
Indus Marine A-1-8140	N/A	15.145	58.5	16.5	7.3	3.2	0.9	0.5	0.8	3.2	0.2	0.0	107	105	359	137	215	15	25	91.2	–9.77
Indus Marine A-1-8240	N/A	15.302	57.9	16.1	7.0	3.3	0.9	0.8	0.8	3.0	0.2	0.0	109	116	367	130	225	16	28	90.1	–10.69
*Indus Marine A-1-8340	N/A	15.459	58.1	15.3	6.2	3.0	0.8	0.2	0.9	2.7	0.1	0.0	513	N/A	14,303	N/A	183	N/A	N/A	88.9	–9.97
Indus Marine A-1-8450	N/A	15.631	53.3	12.0	6.2	2.4	0.7	0.8	0.7	2.1	0.1	0.0	2145	90	67,660	102	208	12	23	85.3	0.43
*Indus Marine A-1-8650	N/A	15.945	39.7	7.6	3.9	1.3	0.4	0.5	0.5	1.2	0.1	0.0	6242	92	94,223	91	226	8	17	65.5	–10.03
*Indus Marine A-1-8950	N/A	16.415	48.1	9.1	4.5	1.6	0.5	0.7	0.9	1.5	0.1	0.0	4124	57	95,849	72	279	7	18	77.2	–9.15
*Indus Marine A-1-9170	N/A	16.760	54.5	11.7	5.5	2.2	0.7	0.3	1.0	2.1	0.1	0.0	2369	N/A	84,818	N/A	177	N/A	N/A	87.0	–10.16

Note: Very high Ba values in samples from petroleum well Indus Marine A-1 reflect contamination by Ba-rich drilling mud. Samples identified with an asterisk are not included in the graphs and are not included in our interpretations. The extremely high Ba and Sr concentrations suggest either the presence of an unusual Ba-Sr solid-solution barite mineral or contamination by drilling mud, which may contain brewsterite (a Sr-Ba zeolite). The IODP sample name shows where the sample was collected; for example, sample U1456A-6H-5 145-150 cm was collected from IODP site U1456, hole A, Core 6, Type H, section 5, and sampled interval depth from 145–150 cm. The Indus Marine A1 sample name contains the depth (ft) of each sample. The "total" column includes content of all major elements and trace elements in the table. Some trace elements, if not analyzed, are marked as N/A.

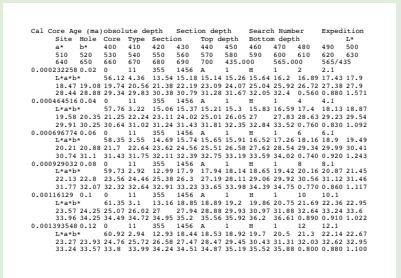

[1]Supplemental Material. Diffuse reflectance spectroscopy (DRS) data from IODP Sites U1456 and U1457 were collected at the Gulf Coast Repository (GCR) in College Station, Texas (USA) using a hand-held Minolta CM-2002 Spectrophotometer. Please visit https://doi.org/10.1130/GEOS.S.13665029 to access the supplemental material, and contact editing@geosociety.org with any questions.

/Homepages/Petschick/MacDiff/MacDiffInfoE.html). For clay minerals present in amounts >10 wt%, the uncertainty is estimated to be better than ±5 wt% at the 95% confidence level. Uncertainty of peak-area measurement based on repeated measurements is typically <5%. High-Ba (>1500 ppm) samples may be contaminated with brewsterite, a common component in drilling mud, so that proxies involving kaolinite are not considered for the oldest five samples from Indus Marine A-1.

Diffuse reflectance spectroscopy (DRS) data are routinely collected by IODP. DRS data were collected at the IODP Gulf Coast Repository (GCR) in College Station, Texas (USA), using a handheld Minolta CM-2002 spectrophotometer. Those data spanning 5.5–8.5 Ma at Site U1456 were already published by Clift et al. (2019a). Sediment reflectance spectra between 390 and 700 nm wavelength range were measured every 2 cm along each core because this range covers most iron oxyhydroxides for mineral reflectance (Deaton and Balsam, 1991). For each measurement, the percent of light intensity reflected from the sample surface was obtained at a 10 nm interval. During data collection, the spectrophotometer was fully in contact with the core surface at the time of measurement. Interference from outside light was avoided in order to increase the accuracy of the reflectance data. The archive half was carefully scraped and rewrapped with Glad plastic cling wrap during the scanning; this wrap is commonly used for shore-based scanning work on IODP and Ocean Drilling Program (ODP) cores (Balsam et al., 1997). Measurements of the sediment spectral reflectance are not distorted as a result, and raw results can be considered reliable. Data are available in the Supplemental Material[1] and at https://data.mendeley.com/datasets/cpnht35vr2/1.

Evaporation during storage resulted in the core surface being drier compared to after initial splitting. Spectral factors analysis indicates that the water content mainly changes the luminance color factor (lightness), which is closely related to the content of carbonate but does not affect our analysis (Giosan et al., 2002a). Deaton and Balsam (1991) have demonstrated that the 565 nm and 435 nm bands are sensitive to the presence of hematite and goethite, respectively. The first-order derivatives of the reflectance intensity of 565 nm and 435 nm were calculated from the data. Because these two minerals are commonly clay sized, their abundance ratio is not affected by grain size. The 565/435 ratio can be used to represent the relative abundance of hematite and goethite with a very high resolution (2 cm). This proxy has a good track

record of showing coherence with other environmentally sensitive indicators (Clift et al., 2014; Liu et al., 2019).

RESULTS

Before using the 565/435 (hematite/goethite) proxy, we need to make sure there is an appropriate level of signal for both of these wavelengths in the scanning data. Figure 2A shows the spectra measured against depth for IODP Site U1456. In general, there is more strength in the signal for the 435 nm (goethite) spectrum compared to the 565 nm (hematite) spectrum, which is almost absent below 600 m below seafloor (mbsf), particularly in the mass-transport deposit. The signal is strongest for both of these wavelengths in the uppermost part of the core, but again with a dominance for goethite, so that the 565/435 (hematite/goethite) proxy is largely controlled by the abundance of that mineral. Comparison with the core descriptions indicates that both minerals, but particularly goethite, are more abundant in the fine-grained sediment interbedded with carbonates compared to in the sandy turbidite deposits.

At IODP Site U1457, we see the strongest development of both 565 nm and 435 nm wavelengths at the top of the section in carbonate-rich, muddy material, and very little hematite is present at the bottom of the core, particularly within the mass-transport deposit (Fig. 2B). There does, however, appear to be a weak signal for 565 nm throughout much of the section. As at Site U1456, the relative intensities of 565/435 are largely controlled by the abundance of goethite. Only in the middle of the core, at ~300–600 mbsf, does it appear that hematite has a stronger signal than goethite.

In terms of long-term trends in magnetic susceptibility (MS) at Site U1456, we observe variable and low values in the mass-transport deposit, with an increase above 750 mbsf and then a slight long-term trend to higher values upsection (Fig. 3). In particular, we note much greater variation and low values of MS above 120 mbsf where the cores contain significant carbonate. There is no clear depth trend in Al/Si. The 565/435 (hematite/goethite) proxy is noisy in the mass-transport deposit but then gradually increases from ~820 to 370 mbsf, above which point it becomes more erratic and declines toward the top of the section. Chemical index of alteration (CIA) values are high in the mass-transport deposit but then decline up-section through the sequence, especially above 750 mbsf and again at 350–400 mbsf. Clay mineralogy shows a dominance of smectite at the base of the drilled section, especially in the mass-transport deposit, although this mineral is present throughout. Illite becomes more dominant upsection, while kaolinite is a minor component of the total throughout. Minor volumes of palygorskite are found in restricted intervals, especially in finer-grained sediments with more carbonate. Illite crystallinity declines upsection, especially above the mass-transport deposit. At the same time, kaolinite/(illite + chlorite) shows a general decrease upsection.

Proxy variations at Site U1457 share some similarities with those at Site U1456 (Fig. 4). Again, MS is lowest in the mass-transport deposit, then increases upsection and shows a series of low-amplitude cycles. The upper 80 m are highly variable in MS and are dominated by muddy lithologies. Si/Al shows no long-term coherent trends, although locally it spikes to higher values, usually in association with sections marked by the frequent presence of sandy turbidite interbeds. These intervals affect all the proxies. 565/435 (hematite/goethite) increases above the mass-transport deposit, with a number of intervals showing lower values, typically in the mud- and carbonate-rich sections. 565/435 values peak ~350 mbsf and then shows a long-term decline trend going upsection, albeit with a secondary peak ~170 mbsf. CIA, illite crystallinity, and kaolinite/(illite + chlorite) show an overall decrease in values upsection. Illite proportions increase upsection, but muddy, carbonate-rich intervals are characterized by higher smectite contents and the presence of small volumes of palygorskite.

DISCUSSION

K/Si and Al/Si Proxies

We can assess the state of chemical weathering of the sediments by comparing K/Si and Al/Si (Lupker et al., 2012). K/Si provides a measure of alteration because K is water-mobile while Si is generally unaffected by chemical weathering. However, this proxy is also affected by grain size, and especially the presence of clay because mudstones are usually more weathered than coarser sandy and silty deposits. Clays are rich in Al while quartz-rich silt and sand have high Si contents, allowing Al/Si to be used as a grain-size proxy. This approach can be used to normalize K/Si to a constant Al/Si value and thus eliminate grain size as an influence over this proxy using the method of Lupker et al. (2012). Figure 5A shows the sediments from the IODP as well as the Indus Marine A-1 boreholes compared with existing analyses from the Quaternary Indus Canyon (Li et al., 2018) and the <14 ka river mouth and/or delta (Clift et al., 2010). Within a given set of data, the overall slope of the array provides a measure of the state of alteration. The Quaternary sediments and the older rocks from Indus Marine A-1 show very similar slopes, suggesting that burial diagenesis has not had a big influence on the composition of the older sedimentary rocks with regard to K and Al. The IODP samples, however, show gentler gradients, indicative of slightly stronger chemical weathering. We compare these analyses with shipboard data from similar sediments recovered from the Bengal Fan (IODP Expedition 354; France-Lanord et al., 2016). The Bengal sediments are comparable to the Indus Marine A-1 material on the K/Si versus Al/Si plot (Fig. 5B) but are moderately less altered than the Laxmi Basin deposits.

Comparing the Indus and Ganges-Brahmaputra basins directly is reasonable because although there might be expected to be a potential provenance effect, this is reduced because of the large size of the catchments, which would tend to drive them toward an upper-continental crustal average. We can compare the bulk composition of the major rivers in both basins using the CN-A-K ([CaO + Na_2O]–Al_2O_3–K_2O) ternary diagram of Fedo et al. (1995) (Fig. 6A). Data are from Alizai et al. (2011) for the Indus and from Lupker et al. (2012, 2013) for the Ganges-Brahmaputra. This plot shows a remarkable

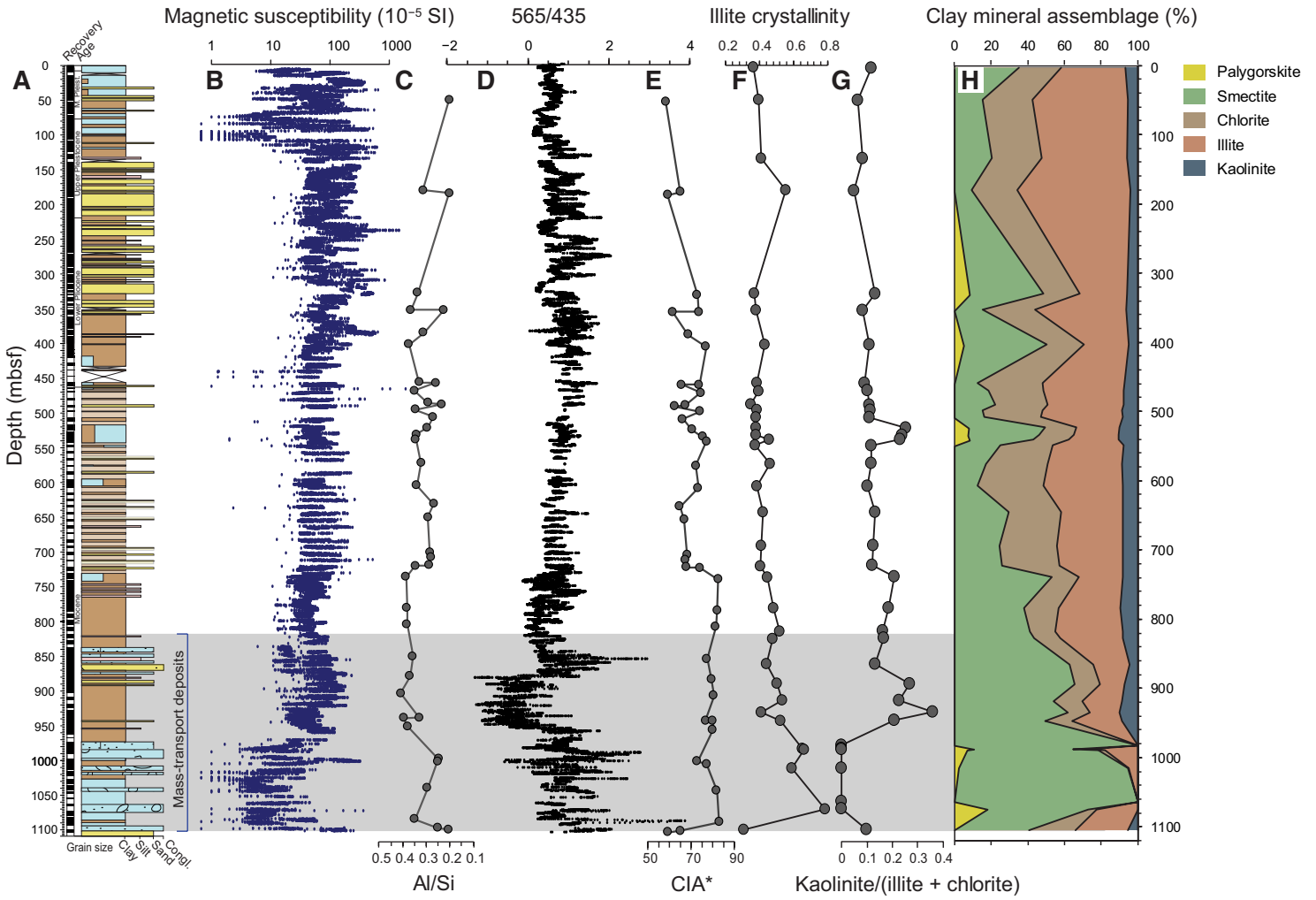

Figure 3. Data from International Ocean Discovery Program Site U1456. (A) Sedimentary log of the drilled section (mbsf—meters below seafloor; M. Pleist.—Middle Pleistocene; Congl.—conglomerate). (B) Magnetic susceptibility. (C) Al/Si. (D) 565/435 hematite/goethite proxy; the first-order derivatives of the reflectance intensity of 565 nm and 435 nm are used to represent the relative abundance of hematite and goethite. (E) Chemical index of alteration (CIA*) with a correction made for excess Ca where appropriate, following the method of Singh et al. (2005). (F) Illite crystallinity. (G) Kaolinite/(illite + chlorite). (H) Clay mineral assemblage.

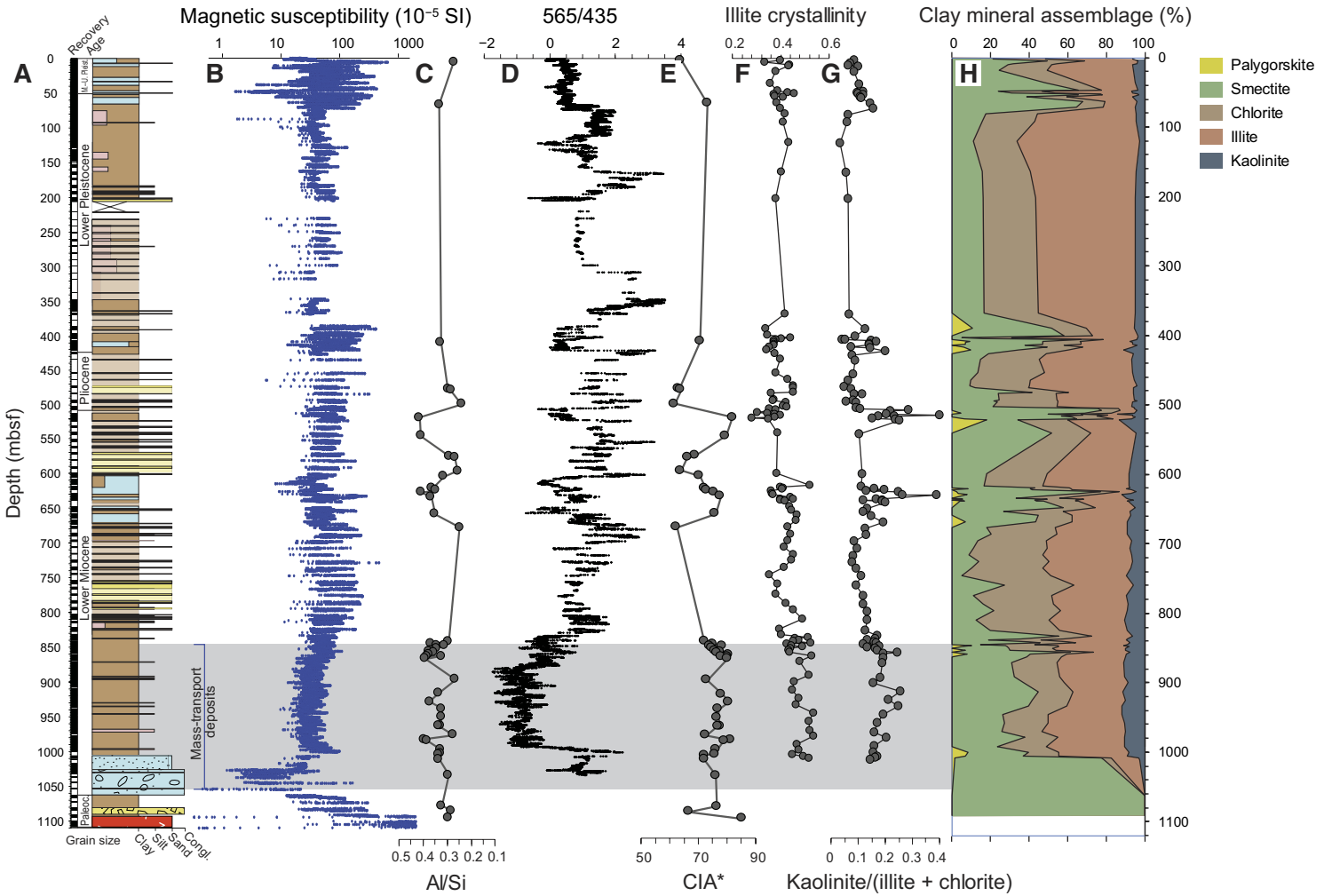

Figure 4. Data from International Ocean Discovery Program Site U1457. (A) Sedimentary log of the drilled section (mbsf—meters below seafloor; Paleoc.—Paleocene; M.-U. Pleist.—Middle to Upper Pleistocene; Congl.—conglomerate). (B) Magnetic susceptibility. (C) Al/Si. (D) 565/435 hematite/goethite proxy. The first-order derivatives of the reflectance intensity of 565 nm and 435 nm are used to represent the relative abundance of hematite and goethite. (E) Chemical index of alteration (CIA*) with a correction made for excess Ca where appropriate, following the method of Singh et al. (2005). (F) Illite crystallinity. (G) Kaolinite/(illite + chlorite). (H) Clay mineral assemblage.

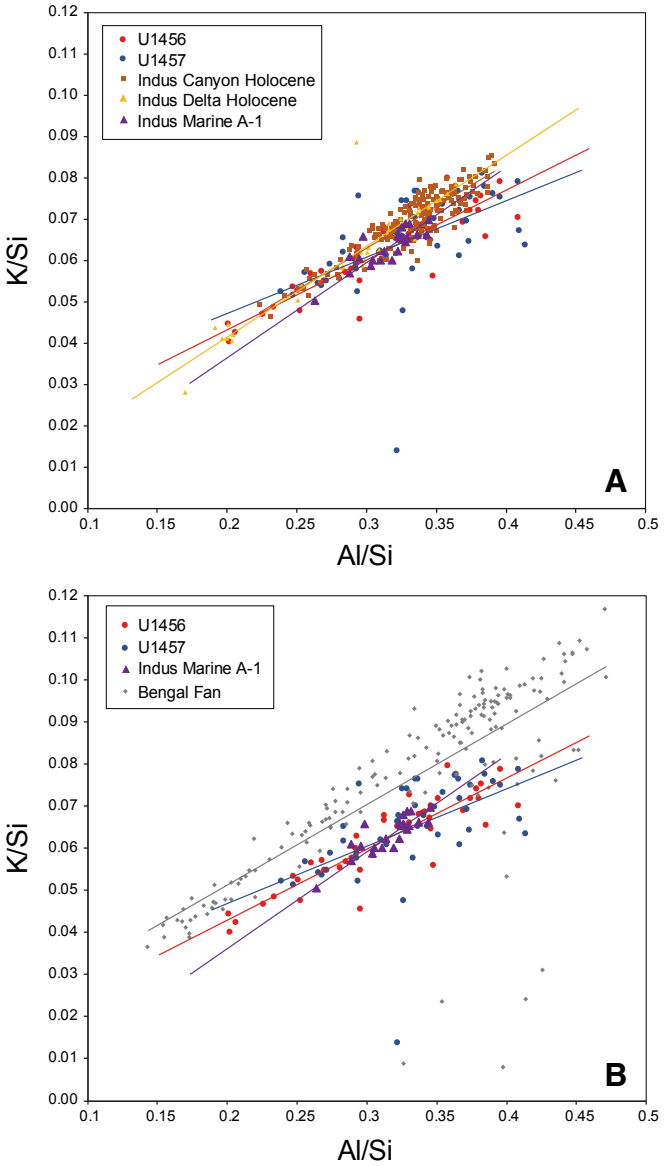

Figure 5. K/Si plotted against Al/Si for Arabian Sea sediments including International Ocean Discovery Program (IODP) Sites U1456 and U1457 as well as the Indus Marine A-1 borehole and Holocene sediments from the Indus Canyon (Li et al., 2018) and onshore delta (Clift et al., 2010) (A), and for IODP Sites U1456 and U1457 and Indus Marine A-1 compared with the Bengal Fan, IODP Expedition 354 (France-Lanord et al., 2016) (B). Trendlines are colored the same as the data series.

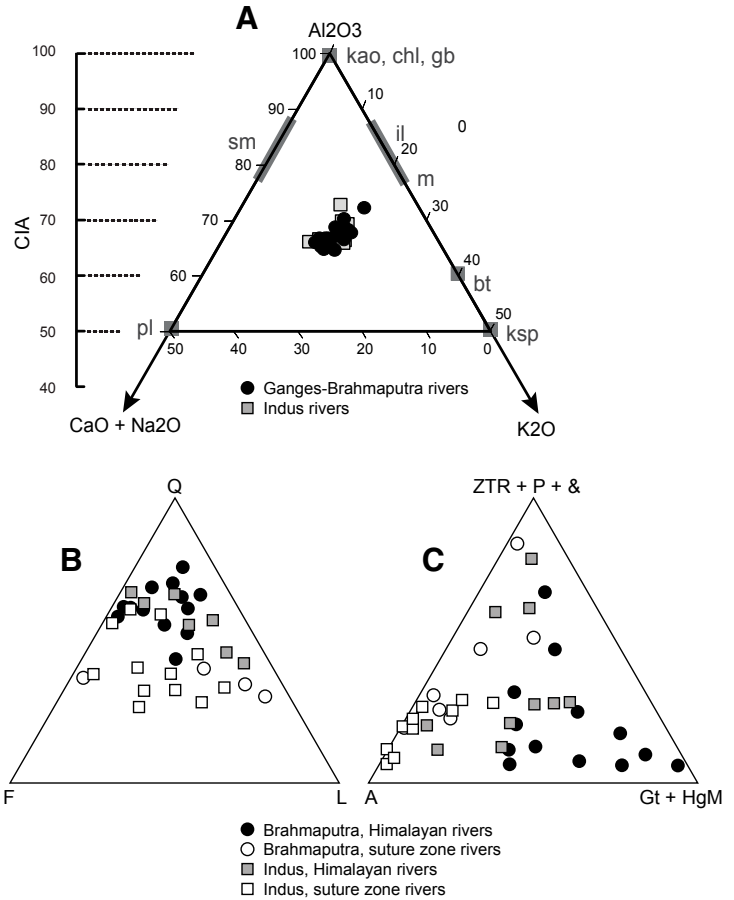

Figure 6. A) Geochemical signature of the bank sediments from Himalayan rivers at the range front illustrated by a CN-A-K ([CaO + Na_2O]–Al_2O_3–K_2O) ternary diagram (Fedo et al., 1995). Indus tributary data are from Alizai et al. (2011); Ganges-Brahmaputra data are from Lupker et al. (2012, 2013). kao—kaolinite; chl—chlorite; Gb—gibbsite; Sm—smectite; Il—plagioclase; pl—plagioclase; il—illite; m—muscovite; bt—biotite; ksp—K-feldspar; CIA—chemical index of alteration. (B) QFL plot and (C) (ZTR + P + &)–A–(Gt + HgM) plot comparing the mineralogy of tributaries in the Indus and Brahmaputra basins draining Himalayan versus suture zone–arc-type source rocks. Q—quartz; F—feldspars; L—total lithics; ZTR—ultrastable minerals (zircon, tourmaline, rutile); P—pyroxenes; &—other dense minerals (mostly sphene or chloritoid); A—amphiboles; Gt—garnet; HgM—high-grade minerals (staurolite, andalusite, kyanite, sillimanite). Indus data are from Garzanti et al. (2005); Brahmaputra data are from Garzanti et al. (2004).

consistency in the composition of the discharge from the mountains. We plot only samples from the river bank at the point where the rivers cross the range front, thus eliminating the effect of weathering in the flood plains. The plot indicates that the raw material supplying both fans is similar in terms of the critical major elements. Furthermore, mineralogical differences are also seen to be modest. The QFL (quartz–feldspars–total lithics) diagram (Dickinson and Suczek, 1979) shows that while suture zone– and Himalaya–draining rivers are different from one another, there is no systematic difference between the two drainage basins (Fig. 6B). Similarly, the heavy-mineral assemblages (Fig. 6C) show little consistent difference between Indus and Ganges-Brahmaputra basins, a conclusion in accord with the analysis of Garzanti and Andò (2007).

Indus Basin versus Bengal Fan

The discrepancy in chemical alteration between the IODP samples and other Indian Ocean sediments is noteworthy. The overall drier conditions in the Indus Basin compared with the Ganges-Brahmaputra would cause slower rates of chemical weathering (Kump et al., 2000; West et al., 2005), while the temperature difference would not be significant and is unlikely to have caused the contrasting trends. Furthermore, fast rates of alteration need not generate more-altered sediment because this depends also on the duration of alteration. If sediment transport was slower from source to sink in the Indus catchment as a result of the lower discharge and stream power, then this could result in deposition of more-altered sediments. However, the fact that Indus Marine A-1 borehole samples and the Quaternary sediments are not also more weathered makes this argument hard to sustain unless weathering was generally more intense in the Indus Basin over the time of the IODP sedimentation (since 10.8 Ma) than during the Quaternary. This is quite possible because the climate has been generally colder and drier since the onset of NHG compared to the deeper past because of the weakening of the summer rains during glacial times (An et al., 2011; Clemens and Prell, 2007; Gupta and Thomas, 2003), the opposite of what has been inferred in Southeast Asia (Zhang et al., 2009).

The sediments of the Indus Marine A-1 borehole are, for the most part, somewhat older than those of the IODP cores, spanning back to 16.7 Ma (early Miocene) when global climate was warmer (Zachos et al., 2001) and potentially wetter because of the intensified hydrologic cycle associated with higher temperatures (Sjolte and Hoffmann, 2014; Webster et al., 1998; You et al., 2009). Alternatively, the geochemical data may suggest that more-weathered sediment is transported to the deep water and not preserved on the shelf. Greater alteration of sediment in the deep-water basin seems less likely because this should have influenced the Bengal Fan as well.

Another factor driving the difference may be sediment flux from western India to the Laxmi Basin, which would not influence the drill sites closer to the Indus River mouth. Rivers such as the Tapti and Narmada (Fig. 1) lack rock uplift, and subtropical conditions would favor strong chemical weathering, as evidenced by the development of thick laterite deposits, especially in the regions of the Deccan Plateau (Maclaren, 1906). Addition of this more-altered material could have influenced the Laxmi Basin sediments. Nd isotope evidence suggests that such sediment supply does take place (Khim et al., 2019; Yu et al., 2019), although generally only since the onset of NHG and so cannot explain differences in older sediments.

Sediment Provenance and Major Elements

We further examine the major element geochemistry using the CN-A-K ternary diagram of Fedo et al. (1995) (Fig. 7). This compares the major element chemistry with the end-member compositions of various weathering products. Unweathered materials plot toward the base of the diagram, with more weathered nearer the top apex. The IODP samples plot largely in an

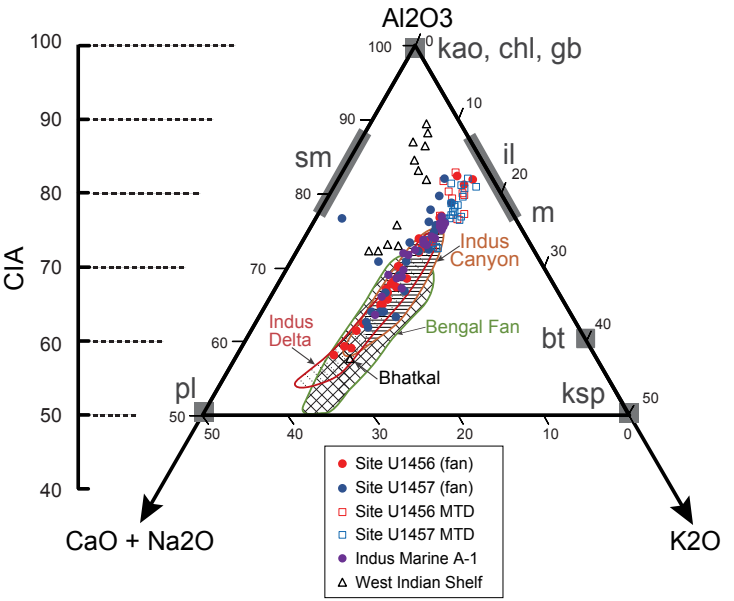

Figure 7. Geochemical signature of the analyzed samples illustrated by a CN-A-K ternary diagram (Fedo et al., 1995). CN denotes the mole weight of Na_2O and CaO* (CaO* represents the CaO associated with silicate, excluding all the carbonate); A and K indicate the content of Al_2O_3 and K_2O, respectively. Samples closer to Al_2O_3 are rich in kaolinite (kao), chlorite (chl), and/or gibbsite (gb). Chemical index of alteration (CIA) values are also calculated and shown on the left side. Other mineral abbreviations: sm—smectite; pl—plagioclase; il—illite; m—muscovite; bt—biotite; ksp—K-feldspar. International Ocean Discovery data from Sites U1456 and U1457 and from the Indus Marine A-1 borehole are compared with data from Holocene sediments from the Indus Canyon (Li et al., 2018) and onshore delta (Clift et al., 2010), as well as modern shelf sediments from western India (Kurian et al., 2013). MTD—mass-transport deposit.

array trending from the lower left toward the illite end member, consistent with the observed clay mineralogy. Although there is overlap, we note that the fan sediments generally plot lower than and to the left of the mass-transport deposits from the same sites (Dailey et al., 2019). Most of the IODP samples plot within the range seen in the Quaternary Indus Canyon and Indus Delta, although they tend to plot at the more weathered end of that range. As seen in the K/Si versus Al/Si plot (Fig. 5), the Laxmi Basin sediments plot within the range of, but also with more altered compositions than, Bengal Fan sediments.

The IODP sediments can also be compared with those from the modern western Indian shelf (Kurian et al., 2013). We consider only those sediments as far south as Bhatikal (Fig. 1) because those further south are of a different composition and, given the south-directed longshore current, extremely unlikely to have been redeposited into the Laxmi Basin close to the drilling sites. Many of the sediments on the northern part of the shelf receive sediment eroded from the Deccan Plateau and plot trending toward the apex of the CN-A-K plot, or to the left of the fields representing the Quaternary delta and canyon. They do not overlap with the IODP samples, indicating that if there is an influence from the western margin, then it has never been dominant. IODP sediments from the mass-transport deposit have the closest association with the western-shelf sediments, consistent with the origin of the deposit from the western shelf of Saurashtra (Calvès et al., 2015). The range of CIA values derived from the plot for Indus Fan sediment is from 56 to 81, representing a wide range of alteration states.

We consider the temporal evolution in the CIAs in Figure 8. We plot a five-point running average to look at the long-term evolution because there is a significant amount of scatter in much of the data at the IODP boreholes. The trends are not noticeably different when plotting four- or six-point moving averages. Data from the Indus Marine A-1 borehole, with the exception of the suspect high-Ba samples, are, in contrast, more stable, possibly because of less grain-size variability, given that these sediments were all shales. We see generally high CIA values from 15 to ca. 9 Ma with a peak from 11 to 9 Ma, then a decline, especially between 9 and 8 Ma (Fig. 8B). A further sharp decrease is noted after 4 Ma, with the lowest values seen in the Pleistocene, which are comparable to CIAs of Holocene sediments in the Indus Canyon (Li et al., 2018). Average CIA values were 77.6 ± 3.5 (1σ) from 10.8 to 9 Ma but decreased to 69.2 ± 5.6 from 3 to 6 Ma and to 66.4 ± 5.9 Ma since 3 Ma. We infer this to indicate reduced chemical alteration through time, although with the sharpest decline between 9 and 6 Ma. The K/Si* proxy is the normalized K/Si by using the method of Lupker et al. (2012), which eliminates the influence of grain size. This proxy shows no clear temporal evolution, although there is a drop in the degree of alteration ca. 11 Ma (Fig. 8C). The high K/Si* values before 15 Ma are likely due to drilling-mud contamination. In contrast, there is a more coherent temporal increase in Na/Si from ca. 10 Ma to the present day, indicating that this is the proxy driving the variations in CIA. The deep-water sediments show higher K/Si* and Al/Si (Fig. 8E) values than the Holocene canyon sediments, although this mostly reflects the generally fine-grained character of the Holocene deposits compared to the deep-water basin sediments. Na is more mobile and more affected by weathering than K, so the lack of signal in K/Si suggests that alteration was variable but not very strong.

In general, the decreasing intensity of chemical alteration can be correlated with the gradual cooling of the global climate since the middle Miocene (Zachos et al., 2001). The humidity index 565/435 is quite variable at IODP Site U1457 (Fig. 8A), but the record at Site U1456 implies a steady increase in aridity or seasonality through the Miocene (Clift et al., 2019a), which would also be consistent with formation of less-altered sediment as drier conditions slowed alteration rates. 565/435 values at both sites imply a peak in aridity in the late Pliocene to early Pleistocene (Fig. 8A) coincident with deposition of sediments with low CIA values. The 565/435 proxy at both sites became more variable during the Pliocene (<4 Ma), possibly linked to the onset of the high-amplitude climate cycles driven by NHG.

Clay Minerals and Environmental Conditions

We also compare the clay mineralogy of the sediments in the boreholes with the Quaternary samples from the Indus Delta and Indus Canyon (Fig. 9). The older samples from the boreholes overlap significantly with the data from the delta and canyon, although these samples also scatter to assemblages with more smectite as well as ones with more illite and chlorite. The IODP samples typically contain slightly more kaolinite than Quaternary sediments from the proximal Indus, suggestive of stronger chemical weathering in the past or the effects of diagenesis. Given the 5% uncertainty in the method, many of the IODP samples are within error of the Quaternary sediments. Sediments older than 8 Ma are more enriched in kaolinite, especially those from the mass-transport deposit and the high-Ba samples from the Indus Marine A-1 borehole.

In order to see how closely coupled the clay mineral and geochemical weathering proxies are, we plot illite crystallinity against CIA (Fig. 10). This comparison shows that there is a rather weak positive correlation between these proxies at both of the IODP sites as well as at the Indus Marine A-1 borehole (R^2 is 0.4197 at Indus Marine A-1, but only 0.116 at Site U1456). R^2 is 0.0009 at Site U1457, indicating no correlation between illite crystallinity and CIA. Calculating P values for these sites indicates that there is no statistically significant correlation between CIA* and illite crystallinity at Sites U1456 and U1457, but that there is a correlation at Indus Marine A-1 ($P = 0.0011$, where $P < 0.05$ indicates correlation). This means either that the proxies have different degrees of sensitivity to chemical weathering, or that other processes are also influencing the value of the proxies, most notably provenance.

Illite crystallinity is seen to be relatively stable from 16 to 11 Ma (Fig. 11). There was a gradual decrease in illite crystallinity from 11 to 5 Ma. Average illite crystallinity is 0.43 ± 0.05 (1σ) from 10.8 to 9.0 Ma but decreases to 0.38 ± 0.05 by 3–6 Ma and it has been only slightly greater than 0.39 ± 0.03 since 3 Ma. Crystallinity values are low and variable during the Plio-Pleistocene, albeit slightly more elevated than in Holocene sediment in the Indus Canyon (Li et al., 2019). When considering kaolinite/(chlorite + illite), we notice a more

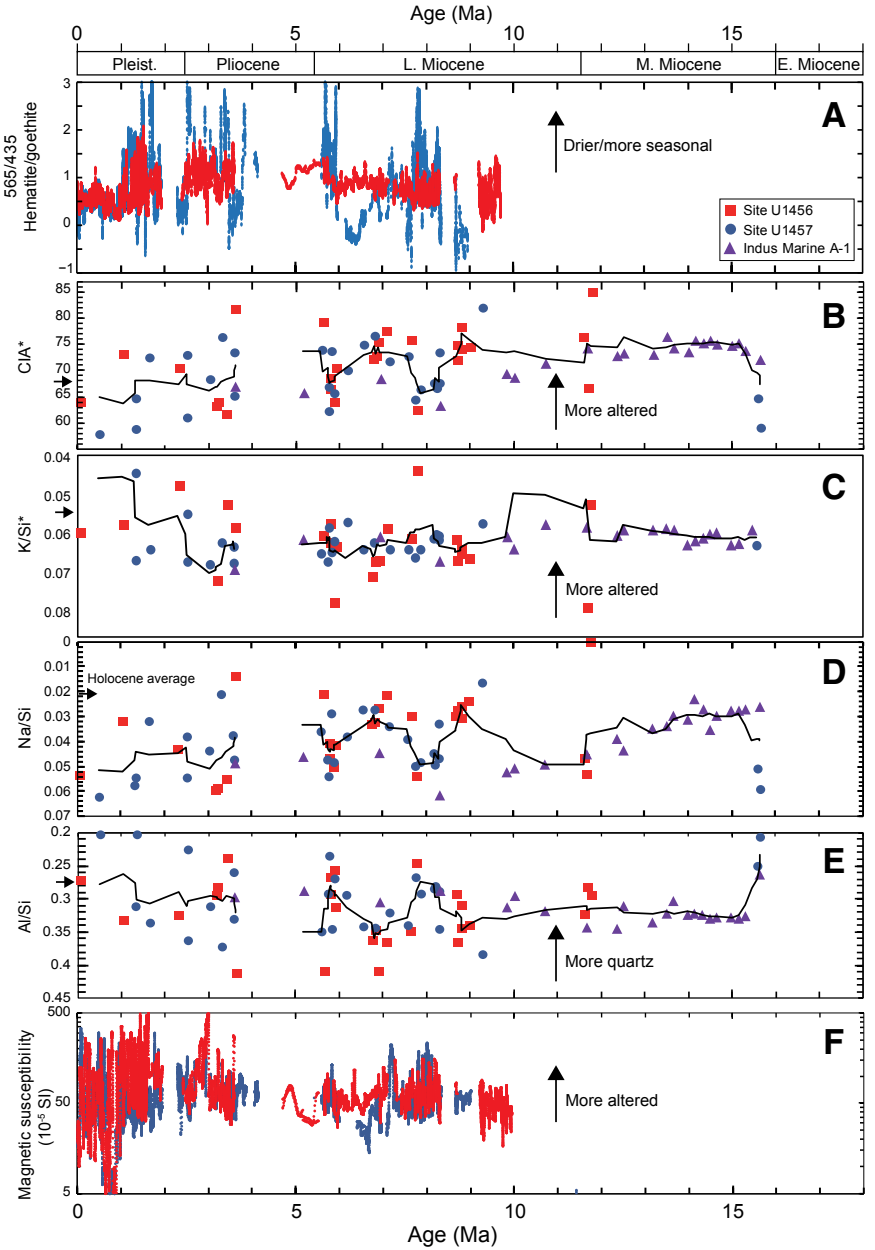

Figure 8. Temporal evolution in geochemical, spectral, and magnetic weathering proxies since 18 Ma at International Ocean Discovery Program Sites U1456 and U1457 and the Indus Marine A-1 borehole. (A) 565/435 hematite/goethite proxy. The first-order derivatives of the reflectance intensity of 565 nm and 435 nm are used to represent the relative abundance of hematite and goethite. (B) Chemical index of alteration (CIA*) calculated by the method of Singh et al (2005). (C) K/Si* eliminate the grain size effect by using the methods of Lupker et al. (2012). (D) Na/Si. (E) Al/Si. (F) Magnetic susceptibility. Thin dark lines in panels B–E are smoothed curves of each data set. Holocene average values shown by horizontal black arrows are from the Indus Canyon data of Li et al. (2018): CIA* = 67.7; K/Si* = 0.0545; Na/Si = 0.0225; Al/Si = 0.2764. L.—late; M.—middle; E.—early.

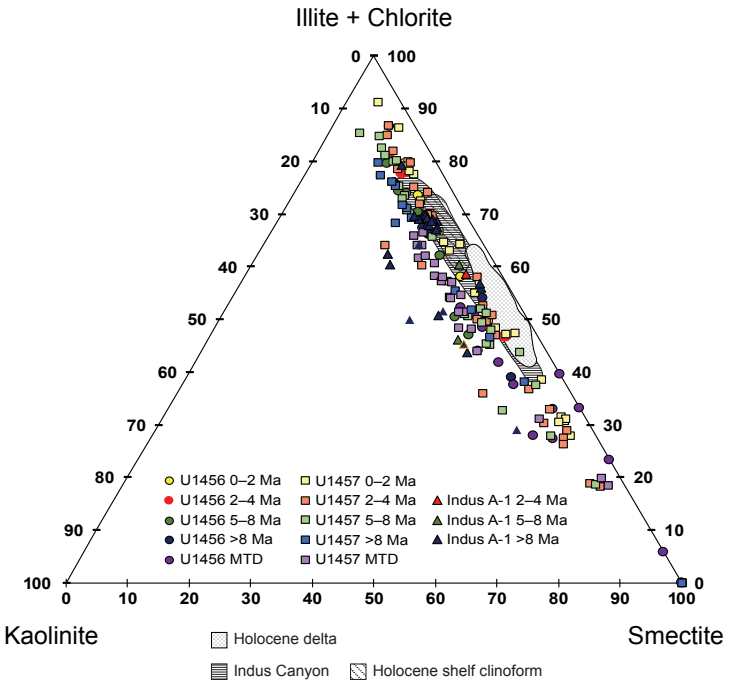

Figure 9. Ternary plot showing the clay mineral assemblages for International Ocean Discovery Program Sites U1456 and U1457 and the Indus Marine A-1 borehole, color coded to show depositional age. Data are compared with data from the Holocene onshore delta (Alizai et al., 2012), the Holocene Indus Canyon (Li, 2018), and the Holocene shelf clinoform (Limmer et al., 2012). MTD—mass-transport deposit.

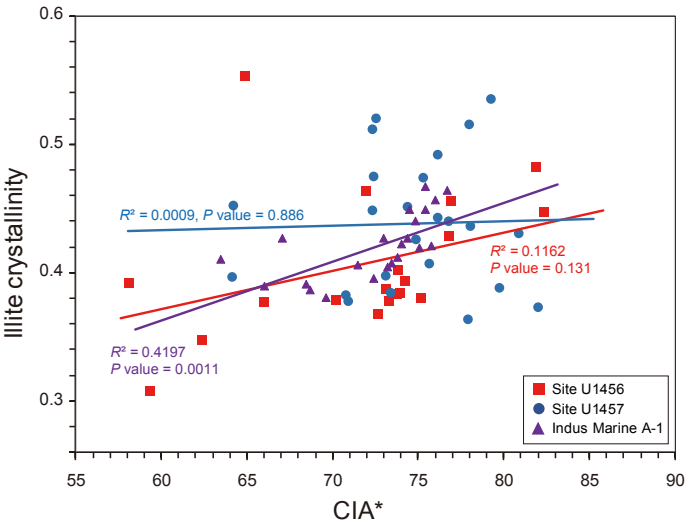

Figure 10. Cross plot of illite crystallinity versus chemical index of alteration (CIA*) (Singh et al., 2005) for International Ocean Discovery Program Sites U1456 and U1457 and the Indus Marine A-1 borehole. The CIA* calculated with a correction made for excess Ca where appropriate, following the method of Singh et al. (2005). Trendlines are colored the same as the data series. Note the rough positive correlation.

significant offset between the more proximal sediments of the Indus Marine A-1 borehole and those of the IODP drill sites in the Laxmi Basin (Fig. 11C). This proxy indicates modestly decreasing chemical weathering between 15 and 11 Ma. The sharp decrease from 16 to 14 Ma is likely a reflection of drilling-mud contamination at the base of the section. There is an increase after 11 Ma, with peaks ca. 10 and ca. 7 Ma. There is a sharp decrease in the index at 3.5 Ma, with low values after that time (average 0.098 ± 0.149, compared to 0.208 ± 0.080 from 6 to 3.5 Ma), similar to values in the Holocene Indus Canyon (Li et al., 2019). Kaolinite/smectite is quite variable but is on average lowest (i.e., least tropical) since 3 Ma (average 0.217 ± 0.145), after being generally higher before 6 Ma (0.411 ± 0.329).

Taken together, the illite crystallinity and kaolinite/(chlorite + illite) proxies indicate reduced degrees of chemical weathering since 3.5 Ma when NHG started (Raymo, 1994). There is also a trend toward less alteration (i.e., less chemical weathering) from 11 to 5 Ma. Prior to 11 Ma, the two proxies support there having been less chemical weathering. The kaolinite/smectite proxy shows little coherent long-term variability except after 3.5 Ma when the weathering became more smectite dominated and potentially more seasonal and less tropical. The fact that this change at 3.5 Ma also coincides with a change in provenance as tracked by Nd isotopes (Fig. 11E) raises the possibility that this is not simply a response to climate forcing. However, the change in Nd isotopes is linked to more erosion from the Lesser Himalaya compared to the Greater Himalaya and Karakoram (Clift et al., 2019b). Because the Lesser Himalaya comprise more sedimentary rocks than the dominantly high-grade metamorphic and igneous rocks of the Greater Himalaya and Karakoram terrains, which are dominantly high-grade metamorphic and igneous rocks, it might be anticipated that alteration would have increased rather than decreased as a result of changing provenance. The fact that this is the opposite of what is observed makes it more likely that the change is driven by environmental factors.

We assess the potential impact of sediment source variations as being the cause of temporal variability in the clay mineralogy. We use Nd isotopes as a proxy for source because they are effective discriminators in this basin (Clift et al., 2002) as well as in many other parts of the world. Fine-grained sediments dominate the bulk isotopic composition of sediment in the Indus (Jonell et al., 2018) so that the clay mineral assemblage might be expected to be closely linked to the isotope composition (Fig. 12). Nd isotopes have moreover already been employed at the IODP sites to reconstruct evolving sources since the mid-Miocene (Clift et al., 2019b). Smectite/kaolinite does

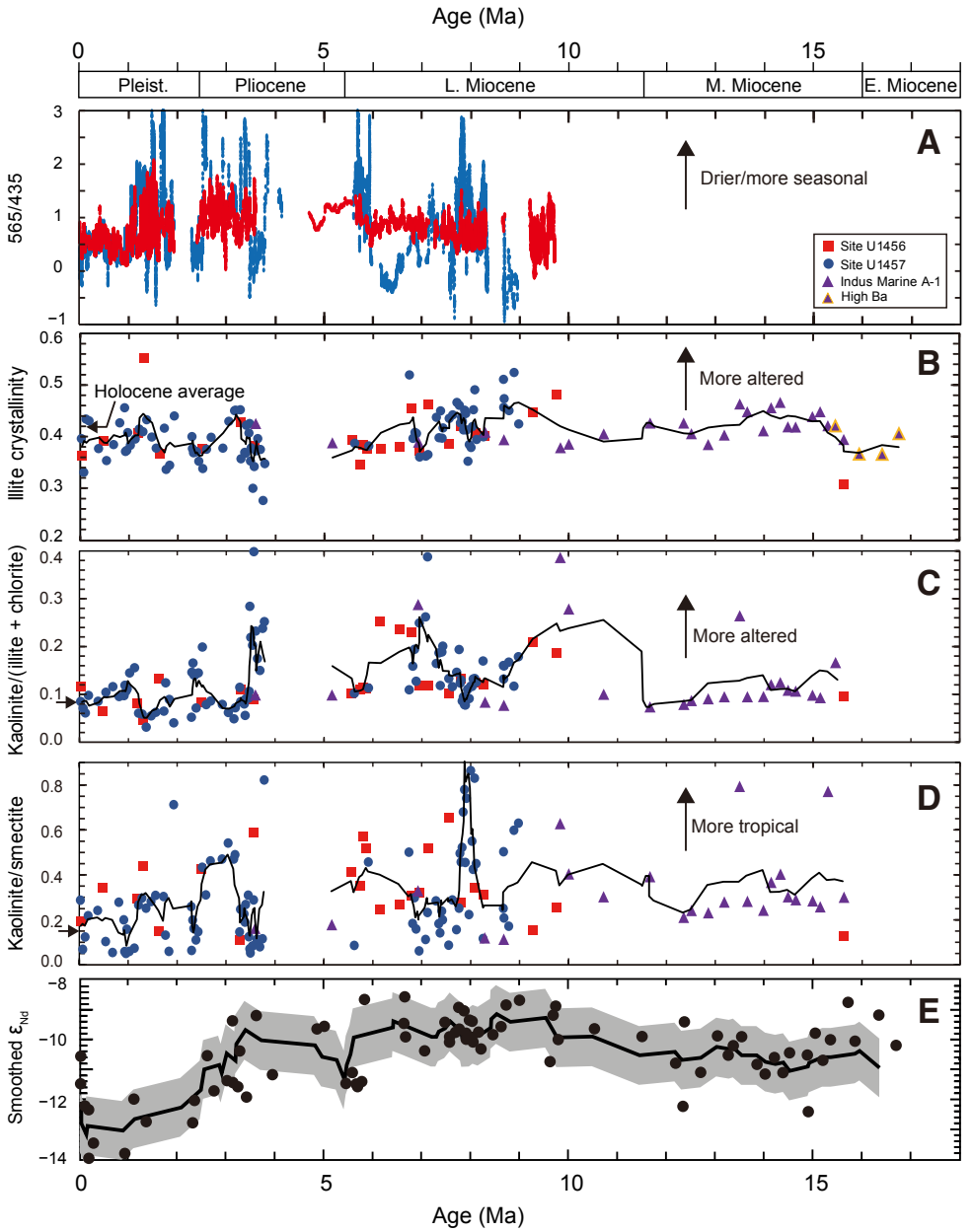

Figure 11. Temporal evolution in clay mineral and spectral proxies since 18 Ma at International Ocean Discovery Program Sites U1456 and U1457 and the Indus Marine A-1 borehole. (A) 565/435 hematite/goethite proxy. The first-order derivatives of the reflectance intensity of 565 nm and 435 nm are used to represent the relative abundance of hematite and goethite. (B) Illite crystallinity. (C) Kaolinite/(illite + chlorite). (D) Kaolinite/smectite. (E) Single-sample (black circles) and smoothed ε_{Nd} values with five-point running average (solid black line) plotted with the ±1ε_{Nd} uncertainty (gray shading) from Clift et al. (2019b) as a proxy for sediment provenance. Holocene average values shown by horizontal black arrows are from the Indus Canyon data of Li et al. (2019): illite crystallinity = 0.42; kaolinite/(illite + chlorite) = 0.0801; kaolinite/smectite = 0.184. L.—late; M.—middle; E.—early.

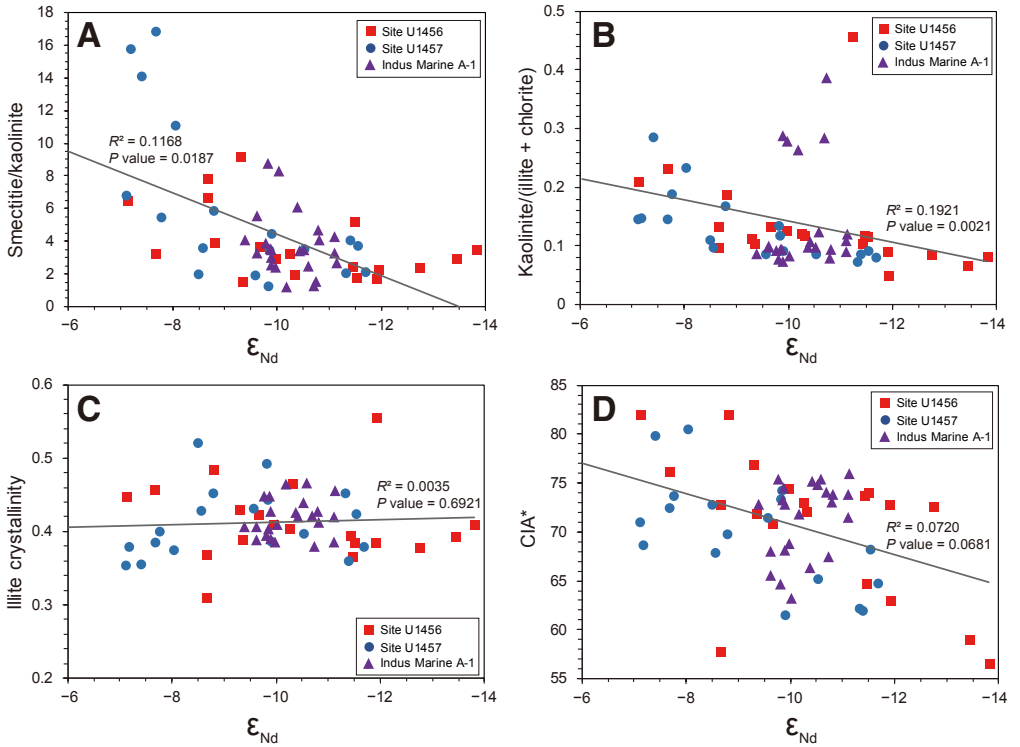

Figure 12. Plots testing for links between provenance (represented by ε_{Nd}) and clay mineral assemblage at International Ocean Discovery Program Sites U1456 and U1457 and the Indus Marine A-1 borehole. (A) ε_{Nd} versus smectite/kaolinite. (B) ε_{Nd} versus kaolinite/(illite + chlorite). (C) ε_{Nd} versus illite crystallinity. (D) ε_{Nd} versus chemical index of alteration (CIA*). Grey trendline represents the trend of both IODP sites and Indus Marine A-1 data.

not show a close correlation with ε_{Nd} value, which is a chondrite-normalized representation of the $^{143}Nd/^{144}Nd$ composition (DePaolo and Wasserburg, 1976) (Fig. 12A). However, the very highest smectite/kaolinite values are associated with the most positive ε_{Nd} values, which may be linked to sediment flux from peninsular India and particularly from the isotopically primitive Deccan Plateau volcanic rocks (Khim et al., 2019; Yu et al., 2019). The samples with the highest ε_{Nd} values do not have a uniform age range and are scattered through the section (Table 2). Although $R^2 = 0.1168$, the *P* value is 0.0187, which is low enough to indicate a statistically significant correlation at 95% confidence. Kaolinite/(chlorite + illite) shows a stronger relationship with ε_{Nd} values ($R^2 = 0.1921$, and a *P* value of 0.0021 indicating significance; Fig. 12B), although higher values are seen when ε_{Nd} is >–9. Peak kaolinite/(chlorite + illite) values are recorded in the older sediments in the Indus Marine A-1 borehole, which generally have intermediate ε_{Nd} values. In this case, the high kaolinite/(chlorite + illite) values may simply reflect stronger chemical weathering at the time of sedimentation and are not obviously linked to provenance. Illite crystallinity (Fig. 12C) shows no dependence on provenance ($R^2 = 0.0035$), with a high *P* value of 0.6921 indicating no significant correlation. CIA* has a weak correlation to ε_{Nd}, i.e., provenance ($R^2 = 0.0720$), with more-weathered samples associated with higher ε_{Nd} values, i.e., potentially more Deccan Plateau derived (Fig. 12D). A *P* value of 0.0681 indicates this correlation is not significant at the 95% confidence level. In general, none of the weathering proxies correlate very well with provenance as tracked by Nd isotopes.

Synthesis

If we consider our most reliable, moderately variable chemical weathering indices, then we can see a significant parallel development between illite crystallinity and CIA* (Fig. 13). We prefer illite crystallinity as a weathering proxy because it shows a coherent variation and does not have the sensitivity to provenance variations seen in the other clay mineral ratios. The downward trend in the past 6 m.y. is also consistent with the Holocene values from the Indus Canyon, suggesting that it is not influenced by current transport or grain-size issues. Likewise, the CIA* is both more coherent and consistent with Holocene values than alternative geochemical proxies. Both of these

TABLE 2. CALCULATED CLAY MINERAL ASSEMBLAGES DERIVED FROM X-RAY POWDER DIFFRACTION ANALYSIS

Sample name	Depth below top of core section (cm)	Age (Ma)	Smectite (%)	Chlorite (%)	Palygorskite (%)	Illite (%)	Kaolinite (%)	Illite FWHM	Illite crystallinity	Illite chemical index	ε_{Nd}
U1456A-1H-2	145–150	0.033	34.8	22.7	0.0	35.0	6.7	0.260	0.364	0.285	–11.49
U1456A-6H-5	145–150	0.476	15.1	27.0	0.0	51.8	5.1	0.283	0.392	0.220	–13.46
U1456A-15H-5	129–134	1.186	20.2	26.8	0.0	46.0	5.9	0.296	0.408	0.263	–13.83
U1456A-25F-3	75–80	1.308	9.2	24.8	0.0	60.9	4.0	0.416	0.553	0.165	–11.96
U1456A-58F-1	89–99	1.631	39.8	19.8	8.1	25.4	6.0	0.262	0.368	0.352	–8.68
U1456A-63F-1	140–150	2.494	15.2	28.0	0.0	49.1	6.5	0.270	0.377	0.271	–12.76
U1456A-72X-4	140–150	3.290	44.0	19.5	5.1	24.0	4.9	0.313	0.429	0.346	–9.30
U1456C-45X-2	111–121	3.565	12.0	35.1	0.0	44.0	7.1	0.275	0.383	0.326	–11.92
U1456D-3R-CC	10–15	5.564	18.1	29.5	0.0	43.2	7.4	0.284	0.393	0.293	–11.45
U1456D-5R-2	94–104	5.736	21.7	28.3	0.0	41.1	7.6	0.246	0.348	0.289	N/A
U1456D-6R-CC	5–10	5.793	14.9	31.8	0.0	42.3	8.5	0.276	0.384	0.304	–11.53
U1456D-7R-1	84–94	5.869	15.9	30.3	0.0	43.9	8.3	0.270	0.377	0.289	N/A
U1456D-8R-5	140–150	6.152	41.1	16.9	8.0	23.3	10.2	0.271	0.378	0.355	N/A
U1456D-9R-5	123–133	6.538	38.6	18.9	7.1	24.3	10.3	0.273	0.380	0.370	N/A
U1456D-10R-3	135–145	6.790	34.4	19.2	8.2	26.6	10.5	0.335	0.455	0.354	–7.69
U1456D-11R-CC*	WRND	6.948	24.2	28.3	0.0	37.6	7.8	0.267	0.374	0.301	N/A
U1456D-14R-CC	10–15	7.132	16.5	33.1	0.0	39.8	8.6	0.342	0.464	0.313	–10.34
U1456D-17R-CC	10–15	7.552	12.1	35.2	0.0	42.1	7.9	0.278	0.387	0.306	–9.36
U1456D-21R-2	115–130	7.789	29.1	27.9	0.0	33.0	8.0	0.307	0.421	0.333	–9.68
U1456D-26R-CC	5–10	8.091	23.8	30.7	0.0	35.3	8.2	0.295	0.408	0.330	–9.99
U1456D-29R-2	128–143	8.269	25.2	30.6	0.0	34.1	7.8	0.291	0.402	0.328	–10.26
U1456D-30R-CC	0–5	9.268	52.5	15.0	0.0	23.8	8.1	0.328	0.447	0.266	–7.14
U1456D-35R-4	107–122	9.759	37.6	18.7	0.0	33.0	9.6	0.357	0.482	0.271	–8.82
U1456D-39R-1	12–14	9.988	40.9	13.8	0.0	36.8	8.2	0.385	0.516	0.257	N/A
U1456D-40R-1	60–62	10.110	43.1	13.9	0.0	34.1	8.1	0.353	0.477	0.244	N/A
U1456D-43R-7	2–4	10.551	62.2	12.9	0.0	19.9	4.4	0.323	0.441	0.211	N/A
U1456D-47R-4	58–60	10.630	65.2	13.8	0.0	13.4	7.3	0.375	0.504	0.299	N/A
U1456D-50R-1	31–33	10.698	53.8	15.5	0.0	21.9	8.5	0.401	0.535	0.257	N/A
U1456D-51R-6	20–22	10.746	61.4	11.9	0.0	15.8	10.0	0.296	0.408	0.383	N/A
U1456D-53R-1	5–7	10.779	49.1	14.6	0.0	27.0	8.7	0.391	0.523	0.274	N/A
U1456E-5R-2	25–27	10.878	100.0	0.0	0.0	0.0	0.0	N/A	N/A	N/A	N/A
U1456D-57R-7	75–77	10.942	53.1	8.4	10.6	26.5	0.0	0.496	0.650	0.216	N/A
U1456D-58R-2	2–4	10.998	69.9	3.8	6.7	17.5	0.0	0.505	0.661	0.209	N/A
U1456D-61R-1	40–42	12.054	91.9	0.8	2.5	4.8	0.0	0.447	0.591	0.159	N/A
U1456E-14R-1	75–77	14.005	96.9	0.0	0.0	0.0	0.0	N/A	N/A	N/A	N/A
U1456E-16R-2	5–7	14.433	54.8	4.6	18.0	22.5	0.0	0.609	0.786	0.185	N/A
U1456E-19R-CC	5–7	15.628	40.0	25.0	0.0	28.3	5.1	0.213	0.308	0.276	–8.68
U1457A-1H-2	83–87	0.024	20.9	27.4	0.0	44.3	6.2	0.286	0.397	0.251	–10.53
U1457A-1H-5	10–12	0.073	48.8	19.4	0.0	27.5	3.3	0.233	0.332	0.264	N/A
U1457A-1H-CC	7–11	0.119	31.5	22.3	0.0	41.3	3.9	0.318	0.435	0.221	N/A
U1457A-2H-2	45–48	0.183	28.7	22.5	0.0	41.6	6.3	0.315	0.431	0.272	N/A
U1457A-3H-1	30–34	0.378	24.4	24.7	0.0	44.1	5.9	0.271	0.378	0.250	N/A
U1457A-4H-6	70–74	0.541	47.4	19.1	0.0	27.9	4.9	0.251	0.354	0.282	N/A
U1457A-6H-1	2–4	0.683	65.3	12.0	0.0	18.7	3.6	0.277	0.385	0.297	N/A
U1457A-6H-2	53–55	0.810	23.7	22.7	0.0	46.2	6.6	0.312	0.427	0.261	–8.58
U1457A-6H-3	64–66	0.910	30.4	22.5	0.0	39.7	6.1	0.336	0.456	0.242	N/A

(*continued*)

TABLE 2. CALCULATED CLAY MINERAL ASSEMBLAGES DERIVED FROM X-RAY POWDER DIFFRACTION ANALYSIS (*continued*)

Sample name	Depth below top of core section (cm)	Age (Ma)	Smectite (%)	Chlorite (%)	Palygorskite (%)	Illite (%)	Kaolinite (%)	Illite FWHM	Illite crystallinity	Illite chemical index	ε_{Nd}
U1457A-6H-4	72–76	0.928	64.4	12.5	0.0	19.0	3.7	0.266	0.372	0.299	N/A
U1457A-6H-6	9–13	0.954	65.4	12.4	0.0	18.5	3.3	0.268	0.374	0.307	N/A
U1457A-7H-1	2–4	0.975	38.4	20.7	0.0	33.8	6.1	0.296	0.408	0.290	N/A
U1457A-7H-5	135–137	1.026	67.8	11.4	0.0	16.4	4.0	0.276	0.384	0.382	–7.69
U1457A-8H-5	10–12	1.126	64.4	13.8	0.0	16.5	4.7	0.286	0.396	0.352	N/A
U1457A-9H-5	62–64	1.210	17.4	26.3	0.0	50.2	4.6	0.302	0.415	0.218	N/A
U1457A-10H-5	72–76	1.283	15.5	26.8	0.0	51.7	4.6	0.298	0.410	0.226	N/A
U1457A-15F-1	4–6	1.364	10.7	22.5	0.0	62.8	2.7	0.317	0.433	0.126	N/A
U1457B-25F-1	128–130	1.466	15.3	24.2	0.0	53.9	4.3	0.289	0.400	0.171	N/A
U1457C-3R-1	59–61	1.558	15.7	26.8	0.0	51.1	4.9	0.271	0.379	0.215	N/A
U1457C-20R-2	84–86	1.723	16.4	27.6	0.0	49.0	5.0	0.303	0.417	0.225	N/A
U1457C-22R-3	100–104	1.761	40.0	17.8	10.6	24.6	5.3	0.237	0.338	0.302	N/A
U1457C-23R-4	45–49	1.833	57.6	14.7	0.0	23.7	3.4	0.244	0.346	0.277	N/A
U1457C-23R-6	145–149	1.929	5.1	25.3	0.0	64.1	3.6	0.323	0.441	0.132	N/A
U1457C-24R-1	14–16	2.290	15.9	29.6	0.0	49.0	4.1	0.290	0.401	0.245	N/A
U1457C-24R-1	87–89	2.298	66.4	11.7	0.0	17.1	4.2	0.271	0.378	0.299	–7.20
U1457C-24R-3	26–28	2.319	37.4	19.2	9.1	25.7	7.4	0.264	0.369	0.353	N/A
U1457C-24R-4	127–129	2.340	39.0	18.9	6.7	25.7	6.3	0.266	0.372	0.355	N/A
U1457C-24R-6	53–55	2.361	39.0	18.9	6.7	25.7	6.3	0.266	0.372	0.206	N/A
U1457C-25R-1	0–4	2.384	37.3	20.1	0.0	37.3	4.1	0.266	0.372	0.222	N/A
U1457C-25R-2	59–61	2.429	43.0	18.3	6.0	25.5	6.3	0.250	0.353	0.325	-7.12
U1457C-25R-4	145–149	2.512	24.5	25.3	9.6	28.3	10.7	0.239	0.339	0.373	N/A
U1457C-26R-CC	2–6	2.588	18.5	29.4	0.0	44.0	5.8	0.269	0.376	0.267	N/A
U1457C-27R-1	21–23	2.681	14.4	30.2	0.0	47.0	6.7	0.289	0.400	0.277	N/A
U1457C-29R-1	30–32	2.922	13.1	33.5	0.0	44.8	6.2	0.271	0.379	0.287	–11.70
U1457C-30R-1	54–58	3.045	9.6	30.3	0.0	53.2	5.2	0.314	0.430	0.223	N/A
U1457C-31R-1	18–20	3.160	8.6	29.6	0.0	53.4	4.0	0.331	0.451	0.177	N/A
U1457C-31R-2	72–74	3.185	11.9	27.2	0.0	53.6	5.8	0.332	0.452	0.195	–11.33
U1457C-32R-1	6–10	3.278	40.9	18.6	0.0	33.3	5.9	0.333	0.453	0.207	N/A
U1457C-32R-2	56–58	3.293	23.6	29.3	0.0	39.4	5.8	0.254	0.358	0.318	–11.41
U1457C-33R-1	26–30	3.370	24.2	29.4	0.0	39.3	5.5	0.265	0.371	0.303	N/A
U1457C-33R-2	72–76	3.387	21.3	32.4	0.0	40.4	4.1	0.263	0.369	0.299	N/A
U1457C-33R-CC	0–4	3.401	23.2	30.7	0.0	37.8	6.2	0.308	0.422	0.357	–11.55
U1457C-34R-1	52–54	3.456	20.9	32.6	0.0	37.9	6.5	0.295	0.408	0.364	N/A
U1457C-34R-2	34–38	3.467	42.9	21.1	0.0	29.0	5.3	0.311	0.426	0.311	N/A
U1457C-34R-3	82–86	3.484	75.1	10.4	0.0	8.4	5.3	0.251	0.354	0.311	–7.41
U1457C-34R-4	118–122	3.500	77.3	9.6	0.0	8.7	4.0	0.272	0.379	0.246	N/A
U1457C-35R-1	14–16	3.536	63.4	13.8	4.7	12.2	5.3	0.207	0.301	0.444	N/A
U1457C-35R-2	14–16	3.565	49.3	17.2	0.0	18.5	14.2	0.242	0.343	0.492	N/A
U1457C-35R-2	133–135	3.601	67.2	13.1	0.0	13.0	6.1	0.267	0.373	0.361	–8.06
U1457C-35R-3	116–118	3.637	56.1	18.2	0.0	18.1	6.4	0.287	0.397	0.315	N/A
U1457C-35R-5	14–16	3.691	61.2	15.6	0.0	16.9	4.9	0.269	0.376	0.302	N/A
U1457C-35R-6	64–66	3.745	57.8	18.4	6.3	9.8	6.7	0.188	0.278	0.675	N/A
U1457C-35R-7	47–51	3.781	16.0	25.9	17.6	26.3	13.1	0.246	0.348	0.532	N/A
U1457C-38R-1	2–4	5.621	51.5	20.2	0.0	23.3	4.4	0.279	0.388	0.285	N/A
U1457C-44R-1	16–20	5.910	17.9	30.6	0.0	41.6	8.2	0.275	0.383	0.303	N/A

(*continued*)

TABLE 2. CALCULATED CLAY MINERAL ASSEMBLAGES DERIVED FROM X-RAY POWDER DIFFRACTION ANALYSIS (*continued*)

Sample name	Depth below top of core section (cm)	Age (Ma)	Smectite (%)	Chlorite (%)	Palygorskite (%)	Illite (%)	Kaolinite (%)	Illite FWHM	Illite crystallinity	Illite chemical index	ε_{Nd}
U1457C-45R-6	92–94	6.741	16.1	29.8	0.0	43.6	8.0	0.388	0.520	0.247	–8.51
U1457C-46R-1	73–75	6.812	42.5	18.0	0.0	31.0	7.8	0.287	0.397	0.271	N/A
U1457C-46R-2	100–104	6.852	31.9	20.9	8.2	28.3	9.5	0.296	0.409	0.372	N/A
U1457C-46R-3	85–87	6.885	41.1	20.8	0.0	30.8	6.6	0.295	0.407	0.258	N/A
U1457C-46R-5	60–62	6.947	74.3	9.7	2.3	8.5	4.5	0.257	0.361	0.391	N/A
U1457C-47R-1	6–10	7.076	62.3	12.7	3.4	14.1	7.0	0.259	0.363	0.388	N/A
U1457C-47R-1	130–132	7.118	49.7	16.1	7.8	13.7	11.6	0.261	0.366	0.642	N/A
U1457C-47R-5	51–53	7.292	33.0	22.6	0.0	34.3	9.4	0.321	0.438	0.312	N/A
U1457C-47R-6	65–69	7.347	43.3	18.9	5.3	23.4	7.9	0.288	0.399	0.394	–7.78
U1457C-47R-7	0–4	7.376	41.5	20.7	0.0	29.1	5.9	0.331	0.451	0.254	N/A
U1457C-48R-1	31–35	7.410	37.0	20.4	6.2	26.4	8.8	0.287	0.398	0.366	N/A
U1457C-48R-2	4–6	7.426	43.4	17.6	4.0	25.6	8.7	0.304	0.418	0.355	N/A
U1457C-49R-1	46–50	7.552	56.8	16.6	0.0	20.5	4.9	0.319	0.436	0.389	N/A
U1457C-49R-4	132–134	7.626	25.8	30.0	0.0	33.9	7.4	0.324	0.443	0.351	–9.85
U1457C-50R-2	79–81	7.710	44.6	17.0	0.0	30.7	7.0	0.344	0.467	0.291	N/A
U1457C-51R-1	98–100	7.762	35.5	18.4	6.8	27.7	9.0	0.340	0.461	0.336	N/A
U1457C-52R-1	98–100	7.782	17.7	34.3	0.0	36.7	8.8	0.312	0.427	0.351	N/A
U1457C-53R-1	41–43	7.805	19.6	33.4	0.0	35.7	9.0	0.321	0.438	0.340	N/A
U1457C-54R-1	6–8	7.826	12.9	34.9	0.0	43.5	6.7	0.314	0.430	0.313	–9.58
U1457C-55R-1	30–32	7.848	11.0	37.2	0.0	41.8	7.5	0.300	0.414	0.324	N/A
U1457C-56R-1	105–109	7.871	8.3	37.6	0.0	45.2	6.5	0.332	0.452	0.328	N/A
U1457C-57R-1	12–14	7.891	13.3	35.6	0.0	42.7	6.1	0.327	0.445	0.275	N/A
U1457C-58R-1	10–14	7.912	9.8	36.1	0.0	44.4	7.2	0.300	0.414	0.313	N/A
U1457C-59R-1	102–106	7.936	4.8	43.5	0.0	37.1	8.9	0.250	0.353	0.308	N/A
U1457C-60R-4	70–74	7.967	26.5	35.0	0.0	30.1	5.9	0.277	0.385	0.347	–9.91
U1457C-62R-1	75–77	8.001	10.5	39.6	0.0	37.6	9.1	0.272	0.380	0.344	N/A
U1457C-63R-3	92–94	8.028	15.6	35.9	0.0	37.5	8.6	0.306	0.420	0.353	N/A
U1457C-64R-3	90–94	8.050	21.0	33.7	0.0	33.7	8.9	0.333	0.453	0.342	N/A
U1457C-65R-6	44–48	8.080	12.0	36.9	0.0	38.2	10.0	0.365	0.491	0.398	–9.83
U1457C-67R-2	78–82	8.112	19.4	35.2	0.0	34.2	8.7	0.285	0.395	0.358	N/A
U1457C-68R-1	73–75	8.253	54.9	16.7	0.0	21.1	6.4	0.289	0.400	0.353	N/A
U1457C-68R-4	130–134	8.666	35.2	21.9	0.0	33.0	8.8	0.381	0.511	0.313	N/A
U1457C-68R-6	32–34	8.672	18.6	27.0	0.0	43.7	9.3	0.337	0.457	0.270	N/A
U1457C-68R-CC	6–8	8.680	39.4	19.9	0.0	31.5	8.2	0.350	0.474	0.281	N/A
U1457C-69R-1	100–104	8.779	45.0	18.6	0.0	27.6	7.7	0.331	0.451	0.301	–8.80
U1457C-69R-3	42–46	8.884	14.7	27.8	0.0	47.4	8.8	0.392	0.525	0.268	N/A
U1457C-69R-4	104–108	8.975	17.2	27.2	9.9	33.5	10.9	0.310	0.425	0.341	N/A
U1457C-69R-6	13–15	9.058	23.2	26.7	4.8	35.6	8.2	0.325	0.444	0.342	N/A
U1457C-69R-7	112–114	9.163	29.0	22.6	0.0	37.4	9.7	0.365	0.491	0.295	N/A
U1457C-70R-2	12–16	9.297	23.0	23.4	6.7	35.6	10.0	0.322	0.440	0.310	N/A
U1457C-70R-3	131–133	9.455	60.9	12.1	0.0	18.8	7.6	0.315	0.431	0.299	N/A
U1457C-70R-5	95–97	9.612	32.3	18.8	7.6	30.6	9.6	0.319	0.436	0.308	–6.50
U1457C-71R-2	109–111	9.717	38.5	17.9	0.0	33.2	9.7	0.394	0.526	0.300	N/A
U1457C-72R-1	107–109	9.772	30.3	23.2	0.0	34.2	10.8	0.354	0.478	0.304	N/A
U1457C-74R-2	25–27	9.939	31.8	23.1	0.0	33.2	10.3	0.385	0.516	0.328	N/A
U1457C-75R-1	36–40	10.014	36.2	21.0	0.0	33.0	8.4	0.334	0.454	0.272	–8.41

(*continued*)

TABLE 2. CALCULATED CLAY MINERAL ASSEMBLAGES DERIVED FROM X-RAY POWDER DIFFRACTION ANALYSIS (*continued*)

Sample name	Depth below top of core section (cm)	Age (Ma)	Smectite (%)	Chlorite (%)	Palygorskite (%)	Illite (%)	Kaolinite (%)	Illite FWHM	Illite crystallinity	Illite chemical index	ε_{Nd}
U1457C-76R-3	44–48	10.129	44.3	17.9	0.0	25.8	11.2	0.328	0.447	0.319	N/A
U1457C-77R-5	26–30	10.242	41.3	19.2	0.0	28.5	10.1	0.350	0.474	0.314	N/A
U1457C-78R-4	25–27	10.318	39.1	19.9	0.0	28.1	11.9	0.341	0.463	0.298	N/A
U1457C-79R-5	129–131	10.432	26.2	23.1	0.0	37.9	11.7	0.401	0.535	0.298	N/A
U1457C-81R-1	30–32	10.545	27.1	22.2	0.0	39.3	10.4	0.385	0.515	0.283	–9.15
U1457C-82R-3	6–8	10.659	25.5	20.9	0.0	42.6	10.2	0.389	0.520	0.260	N/A
U1457C-83R-2	18–20	10.735	37.7	16.8	0.0	34.1	10.4	0.401	0.535	0.257	N/A
U1457C-84R-3	143–145	10.849	23.1	25.0	0.0	39.9	10.4	0.345	0.468	0.289	N/A
U1457C-85R-3	46–50	10.925	31.1	15.8	8.1	36.2	8.1	0.351	0.474	0.282	N/A
U1457C-86R-1	6–8	10.983	29.6	18.2	6.9	35.3	9.1	0.329	0.448	0.299	N/A
U1457C-86R-2	44–46	11.001	75.5	5.1	1.5	14.4	3.1	0.365	0.492	0.282	N/A
U1457C-87R-1	14–18	11.030	77.0	4.5	1.5	13.6	2.6	0.386	0.517	0.198	–5.48
U1457C-93R-1	50–54	11.500	100.0	0.0	0.0	0.0	0.0	N/A	N/A	N/A	N/A
U1457C-93R-3	50–52	11.527	100.0	0.0	0.0	0.0	0.0	N/A	N/A	N/A	N/A
U1457C-94R-2	55–59	11.597	100.0	0.0	0.0	0.0	0.0	N/A	N/A	N/A	0.33
U1457C-95R-1	12–14	11.666	100.0	0.0	0.0	0.0	0.0	N/A	N/A	N/A	N/A
U1457C-96R-1	62–66	11.756	100.0	0.0	0.0	0.0	0.0	N/A	N/A	N/A	–5.66
Indus Marine A-1-1620	N/A	3.597	35.0	19.6	0.0	38.1	5.7	0.311	0.426	0.168	–10.38
Indus Marine A-1-2200	N/A	5.163	33.0	24.4	0.0	35.1	5.9	0.280	0.389	0.285	–9.62
Indus Marine A-1-3180	N/A	6.926	39.9	16.0	0.0	29.6	13.1	0.281	0.390	0.321	–9.89
Indus Marine A-1-3960	N/A	8.290	38.6	21.4	0.0	33.8	4.6	0.297	0.409	0.231	–10.03
Indus Marine A-1-4180	N/A	8.675	38.1	24.3	0.0	31.6	4.3	0.285	0.395	0.268	–9.81
Indus Marine A-1-4840	N/A	9.830	30.2	13.6	0.0	35.6	19.0	0.272	0.379	0.274	–10.73
Indus Marine A-1-4940	N/A	10.005	34.4	20.2	0.0	29.9	13.9	0.278	0.386	0.308	–9.97
Indus Marine A-1-5360	N/A	10.716	22.8	32.7	0.0	36.0	6.9	0.294	0.406	0.324	–9.62
Indus Marine A-1-5920	N/A	11.665	14.6	36.0	0.0	41.9	5.7	0.311	0.427	0.299	–9.89
Indus Marine A-1-6360	N/A	12.355	25.2	31.6	0.0	35.8	5.3	0.311	0.427	0.316	–10.79
Indus Marine A-1-6460	N/A	12.512	24.4	34.7	0.0	33.2	5.9	0.294	0.406	0.354	–9.38
Indus Marine A-1-6680	N/A	12.857	25.9	32.9	0.0	33.2	6.0	0.277	0.385	0.338	–11.10
Indus Marine A-1-6890	N/A	13.186	23.1	34.6	0.0	33.4	6.4	0.292	0.404	0.347	–9.85
Indus Marine A-1-7090	N/A	13.499	20.5	26.2	0.0	35.3	16.3	0.342	0.464	0.399	–10.18
Indus Marine A-1-7190	N/A	13.656	22.7	34.7	0.0	32.9	6.4	0.329	0.449	0.350	–9.87
Indus Marine A-1-7400	N/A	13.985	25.7	33.4	0.0	32.0	6.2	0.299	0.412	0.355	–10.81
Indus Marine A-1-7500	N/A	14.142	22.0	35.0	0.0	32.2	8.1	0.336	0.456	0.378	–11.14
Indus Marine A-1-7620	N/A	14.330	20.9	34.5	0.0	33.4	8.4	0.344	0.467	0.365	–10.59
Indus Marine A-1-7720	N/A	14.487	23.8	34.0	0.0	32.3	7.2	0.305	0.420	0.369	–11.10
Indus Marine A-1-7820	N/A	14.644	24.2	33.2	0.0	32.6	7.0	0.305	0.419	0.356	–10.42
Indus Marine A-1-8040	N/A	14.989	23.1	32.4	0.0	34.6	6.6	0.322	0.439	0.318	–10.51
Indus Marine A-1-8140	N/A	15.145	24.0	34.2	0.0	32.4	6.2	0.329	0.449	0.374	–9.77
Indus Marine A-1-8240	N/A	15.302	21.8	25.8	0.0	33.3	16.8	0.307	0.422	0.368	–10.69
Indus Marine A-1-8340	N/A	15.459	24.4	31.2	0.0	31.4	10.4	0.307	0.421	0.389	–9.97
Indus Marine A-1-8450	N/A	15.631	42.3	20.6	0.0	22.2	12.7	0.285	0.395	0.302	0.43
Indus Marine A-1-8650	N/A	15.945	56.8	13.1	0.0	15.3	12.0	0.262	0.367	0.283	–10.03
Indus Marine A-1-8950	N/A	16.415	40.9	24.4	0.0	20.1	12.5	0.261	0.367	0.379	–9.15
Indus Marine A-1-9170	N/A	16.760	34.4	26.1	0.0	24.1	12.6	0.294	0.406	0.343	–10.16

*WRND in sample name means samples as whole rounds taken on the catwalk.

Note: FWHM is the full width at half maximum intensity. Illite chemical index refers to a ratio of the 0.5 and 1 nm peak areas. If a sample has no illite content, the illite FWHM, illite crystallinity, and illite chemical index for that sample are marked as N/A. Some samples that have no Nd isotope data are marked as N/A as well.

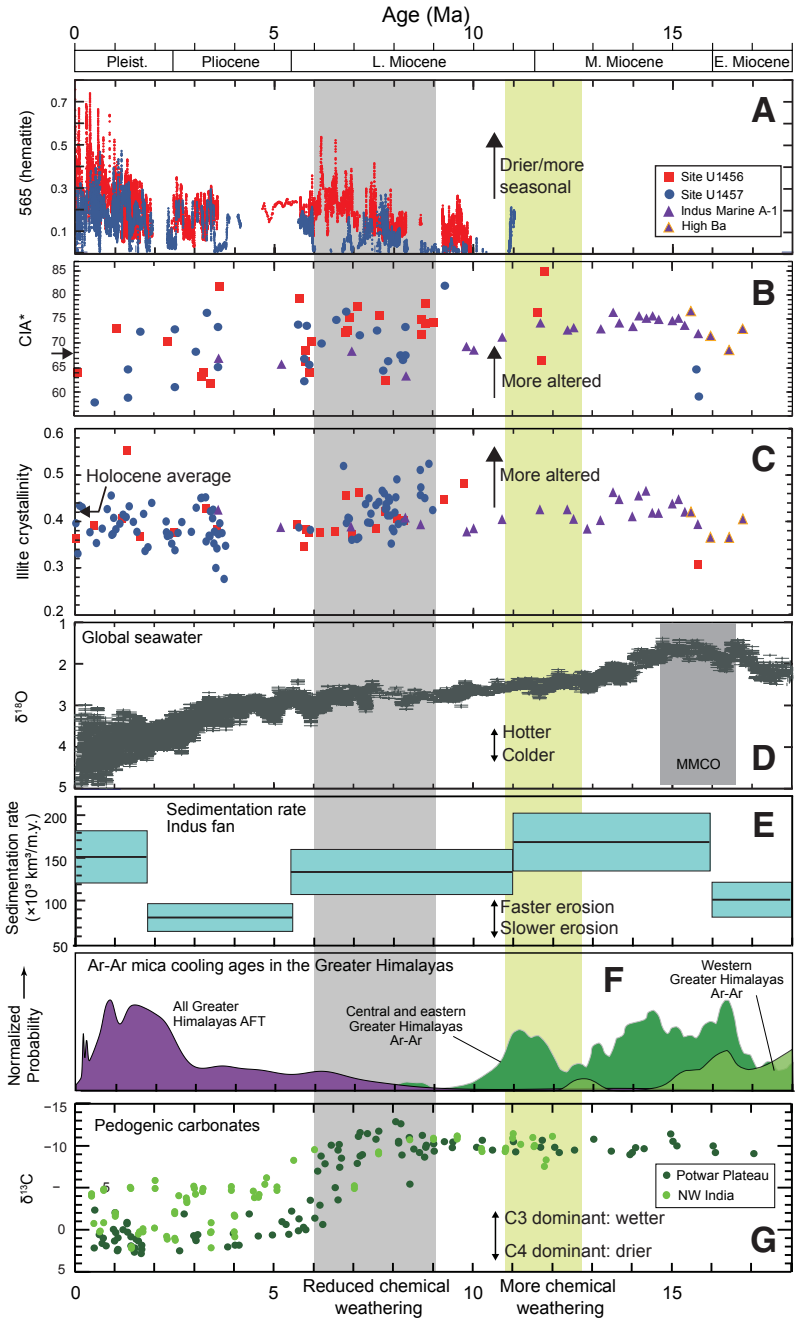

Figure 13. Temporal evolution in weathering proxies for International Ocean Discovery Program Sites U1456 and U1457 and the Indus Marine A-1 borehole, together with possible forcing factors. (A) 565 hematite proxy, the first-order derivatives of the reflectance intensity of 565 nm, used to represent the relative abundance of hematite. (B) Chemical index of alteration (CIA*) following the method of Singh et al. (2005). (C) Illite crystallinity. (D) Global seawater $\delta^{18}O$ as a proxy for seawater temperature (Zachos et al., 2001, 2008). MMCO—Mid-Miocene Climatic Optimum. (E) Sedimentation rates for the Indus Fan (Clift, 2006) shown in black line with turquoise error bars. (F) Probability densities for $^{40}Ar/^{39}Ar$ muscovite dates and apatite fission-track (AFT) dates from the Himalayan hinterland and proximal foreland (Clift et al., 2008b). (G) Pedogenic carbonate $\delta^{13}C$ from the Siwaliks (Quade et al., 1989; Singh et al., 2011). Yellow shaded vertical bar indicates a time of increasing chemical weathering, while the gray shaded bar indicates a time of long-term reduced weathering. Average Holocene values are from the Indus Canyon data of Li et al. (2019) (black horizontal arrows): CIA* = 67.7; illite crystallinity = 0.42. Pleist.—Pleistocene; L.—late; M.—middle; E.—early.

proxies indicate moderately high degrees of alteration from 15 Ma to 11 Ma, and then achieve values indicative of maximum alteration from 11 to 9 Ma. We then see a reduction in alteration from 9 to 6 Ma, followed by a period of relatively low but variable alteration to the present day. Few of these transitions appear to be related to variations in global temperatures, as tracked by foraminiferal oxygen isotopes (Zachos et al., 2008). However, the time of decreasing alteration does correlate with the carbon isotope transition in the foreland basin (Fig. 13G) that has been linked to a change in the vegetation in that region and generally attributed to drier conditions in the flood plains (Clift et al., 2019a; Dettman et al., 2001). This is also a time when sediment flux to the Arabian Sea was decreasing (Clift, 2006) (Fig. 13E). Furthermore, the abundance of hematite as tracked by the strength of the 565 nm diffuse reflectance spectroscopy signal (Fig. 13A) rises significantly at that time, especially in the more continuous IODP Site U1456 record. Because this mineral is associated with weathering in arid or seasonal conditions (Walker, 1967), this is consistent with the reconstruction of a drying climate in the Indus Basin causing reduced chemical alteration. Hematite is also very common in the Pleistocene, reflecting weathering under more arid glacial conditions (An et al., 2011; Clemens and Prell, 2007).

It is harder to assess the importance of the maximum weathering from 11 to 9 Ma, as this is inferred in part from the difference in CIA and illite crystallinity between sediments at the IODP sites at which the record before 10.8 Ma is lost to mass wasting, and those from the Indus Marine A-1 borehole (Pandey et al., 2016c). The difference could represent the difference between proximal and distal records, although the fact that this gradual weakening in alteration is seen in illite crystallinity, where similarly aged samples from proximal and distal sites have similar crystallinity values and provenance, is supportive of the concept that this transition reflects a change in weathering intensity and climate. The poor data coverage from 12 to 10.8 Ma makes the nature of the transition hard to define, and the apparent modest jump in crystallinity values in Figure 11B likely reflects this. This 9–10.8 Ma maximum, following intensification after 13 Ma, is not paralleled in the foreland basin carbon isotope record, which is controlled by flood-plain vegetation, although this period is still recognized as a time of rapid exhumation in the western Greater Himalaya, based on the bedrock compilation of Clift et al. (2008b) and structural reconstructions (Webb, 2013), as well as being a time of rapid sedimentation on the Indus Fan (Fig. 13E). These factors are consistent with ca. 11–9 Ma being a time of strong monsoon precipitation. We reconcile between evidence for changing weathering conditions after 13 Ma despite no change in the flood-plain vegetation, with the idea that vegetation and thus carbon isotopes change only when a threshold value of rainfall is passed. Moderate changes in precipitation intensity do not greatly influence the vegetation in the flood plains and would thus not be recorded in the stable isotope record (Vögeli et al., 2017), although they would be sufficient to impact erosion and weathering rates.

The data presented here show that in the late Miocene, chemical weathering intensity likely decreased, while at the same time sedimentation rates in the Indus Fan also decreased, indicating reduced chemical weathering flux. Even if proxies like K/Si are instead preferred and no resolvable trend with time is concluded, this would still imply a reducing chemical weathering flux in light of slow sedimentation rates in the fan from the middle Miocene to the Pliocene. This trend not consistent with simple models that link long-term global cooling to an increase in chemical weathering in the Himalaya, drawing down atmospheric CO_2 (Raymo and Ruddiman, 1992). The data are, however, consistent with the idea that colder, drier climates slow chemical weathering rates (West et al., 2005), which would generally cause deposition of less-altered material if transport times did not shorten synchronously. The decrease in global temperatures since 5 Ma is not reflected by stronger weathering in the western Himalaya, as recorded in these sites, although sedimentation rates did increase, which would partly or totally compensate for the decline in weathering fluxes. Our data do not prove the Caves et al. (2016) hypothesis that increased land surface reactivity, rather than increasing chemical weathering fluxes, can explain the long-term drawdown in Cenozoic atmospheric CO_2, but the declining chemical alteration documented in this work is consistent with that model in that our evidence argues against a simple, direct link between Himalayan erosion and colder global temperatures. This work does not indicate that the western Himalaya would be the location of increasingly reactive bedrock.

CONCLUSIONS

In this study, we present a multi-proxy chemical weathering reconstruction of the Indus drainage basin dating from 17 Ma, as recovered from the Arabian Sea. Bulk sediment geochemistry and clay mineral assemblages show progressive long-term changes since that time. Chemical weathering appears to have been relatively strong from 17 to 11 Ma. Grain size does not appear to be a major control on the chemical weathering indices. Indus submarine fan sediments are more weathered than those found in the Bengal Fan that span a similar time period. They are also more weathered than Quaternary Indus Fan and Indus Delta sediments. The higher degrees of alteration may reflect longer transport times caused by the lower discharge, despite the drier climate in the Indus Basin compared to the Ganges-Brahmaputra basin. Although clay mineral proxies, such as illite crystallinity, do not correlate closely with geochemical ratios, they do show the same long-term trend toward reduced chemical weathering, particularly between 9 and 6 Ma. This is the same time that the vegetation in the flood plains of the foreland basin changed from being C3 wood-dominated to C4 grass-dominated (Quade et al., 1989). Concentrations of hematite, a mineral associated with formation under arid or at least seasonal conditions, also increased at this time.

Clay mineral proxies show a tendency to be controlled by provenance. In particular, sediment flux from peninsular India may have been important to the supply of smectite, typically during times of lower sea level. Consequently, greater confidence is placed in the illite crystallinity proxy for examining environmental conditions because this is not influenced by these additional

contributions. The weathering record is broadly consistent with a drying climate following the relatively hot and humid environmental conditions in the middle Miocene. This means that the oceanic upwelling and biogenic production record from the Indian Ocean, widely considered to be a proxy record for monsoon wind strength (Kroon et al., 1991), are essentially decoupled from the precipitation history in the Himalaya and their adjacent basins. Additional processes must be controlling the rainfall intensity, probably the cooling global temperatures that reduce the amount of moisture in the atmosphere over time. Declining or at the very least stable chemical weathering intensity in the late Miocene at the same time that sedimentation rates in the submarine fan decreased means that total weathering fluxes must have been declining at this time and cannot have been the mechanism by which atmospheric CO_2 was reduced, which drove long-term global cooling. Such a conclusion is consistent with recent suggestions that increasing land surface reactivity caused by greater fresh-mineral surface area or an increase in the supply of reactive minerals is behind the trend to decreasing atmospheric CO_2 in the Neogene (Caves Rugenstein et al., 2019) rather than a simple increase in chemical weathering in the region of the Himalaya.

ACKNOWLEDGMENTS

This study was made possible by samples provided by the IODP. The work was partially funded by a grant from The U.S. Science Support Program (USSSP), as well as additional funding from the Charles T. McCord Jr. Endowed Chair in petroleum geology at LSU. The work benefited from comments by two anonymous reviewers and editor David Fastovsky.

REFERENCES CITED

Alizai, A., Carter, A., Clift, P.D., VanLaningham, S., Williams, J.C., and Kumar, R., 2011, Sediment provenance, reworking and transport processes in the Indus River by U-Pb dating of detrital zircon grains: Global and Planetary Change, v. 76, p. 33–55, https://doi.org/10.1016/j.gloplacha.2010.11.008.

Alizai, A., Hillier, S., Clift, P.D., Giosan, L., Hurst, A., VanLaningham, S., and Macklin, S., 2012, Clay mineral variations in Holocene terrestrial sediments from the Indus Basin: Quaternary Research, v. 77, p. 368–381, https://doi.org/10.1016/j.yqres.2012.01.008.

An, Z., Kukla, G.J., Porter, S.C., and Xiao, J., 1991, Magnetic susceptibility evidence of monsoon variation on the Loess Plateau of central China during the last 130,000 years: Quaternary Research, v. 36, p. 29–36, https://doi.org/10.1016/0033-5894(91)90015-W.

An, Z., Clemens, S.C., Shen, J., Qiang, X., Jin, Z., Sun, Y., Prell, W.L., Luo, J., Wang, S., Xu, H., Cai, Y., Zhou, W., Liu, X., Liu, W., Shi, Z., Yan, L., Xiao, X., Chang, H., Wu, F., Ai, L., and Lu, F., 2011, Glacial-interglacial Indian summer monsoon dynamics: Science, v. 333, p. 719–723, https://doi.org/10.1126/science.1203752.

Andò, S., Aharonovich, S., Hahn, A., George, S.C., Clift, P.D., and Garzanti, E., 2019, Integrating heavy-mineral, geochemical and biomarker analyses of Plio-Pleistocene sandy and silty turbidites: A novel approach for provenance studies (Indus Fan, IODP Expedition 355): Geological Magazine, v. 157, p. 929–938, https://doi.org/10.1017/S0016756819000773.

Balsam, W.L., Damuth, J.E., and Schneider, R.R., 1997, Comparison of shipboard vs. shore-based spectral data from Amazon Fan cores: Implications for interpreting sediment composition, *in* Flood, R.D., Piper, D.J.W., Klaus, A., and Peterson, L.C., eds., Proceedings of the Ocean Drilling Program, Scientific Results, Volume 155: College Station, Texas, Ocean Drilling Program, p. 193–215, https://doi.org/10.2973/odp.proc.sr.155.210.1997.

Berner, R.A., and Berner, E.K., 1997, Silicate weathering and climate, *in* Ruddiman, W.F., ed., Tectonic Uplift and Climate Change: New York, Springer, p. 353–365, https://doi.org/10.1007/978-1-4615-5935-1_15.

Betzler, C., Eberli, G.P., Kroon, D., Wright, J.D., Swart, P.K., Nath, B.N., Alvarez-Zarikian, C.A., Alonso-García, M., Bialik, O.M., Blättler, C.L., Guo, J.A., Haffen, S., Horozai, S., Inoue, M., Jovane, L., Lanci, L., Laya, J.C., Mee, A.L.H., Lüdmann, T., Nakakuni, M., Niino, K., Petruny, L.M., Pratiwi, S.D., Reijmer, J.J.G., Reolid, J., Slagle, A.L., Sloss, C.R., Su, X., Yao, Z., and Young, J.R., 2016, The abrupt onset of the modern South Asian Monsoon winds: Scientific Reports, v. 6, 29838, https://doi.org/10.1038/srep29838.

Bhattacharya, G.C.B., Chaubey, A.K., Murty, G.P.S., Srinivas, K., Sarma, K.V.L.N.S., Subrahmanyam, V., and Krishna, K.S., 1994, Evidence for seafloor spreading in the Laxmi Basin, northeastern Indian Ocean: Earth and Planetary Science Letters, v. 125, p. 211–220, https://doi.org/10.1016/0012-821X(94)90216-X.

Bickle, M.J., Chapman, H.J., Tipper, E., Galy, A., De La Rocha, C.L., and Ahmad, T., 2018, Chemical weathering outputs from the flood plain of the Ganga: Geochimica et Cosmochimica Acta, v. 225, p. 146–175, https://doi.org/10.1016/j.gca.2018.01.003.

Biscaye, P.E., 1965, Mineralogy and sedimentation of recent deep-sea clay in the Atlantic Ocean and adjacent seas and oceans: Geological Society of America Bulletin, v. 76, p. 803–832, https://doi.org/10.1130/0016-7606(1965)76[803:MASORD]2.0.CO;2.

Blöthe, J.H., Munack, H., Korup, O., Fülling, A., Garzanti, E., Resentini, A., and Kubik, P.W., 2014, Late Quaternary valley infill and dissection in the Indus River, western Tibetan Plateau margin: Quaternary Science Reviews, v. 94, p. 102–119, https://doi.org/10.1016/j.quascirev.2014.04.011.

Bookhagen, B., and Burbank, D.W., 2006, Topography, relief, and TRMM-derived rainfall variations along the Himalaya: Geophysical Research Letters, v. 33, L08405, https://doi.org/10.1029/2006GL026037.

Burbank, D.W., Beck, R.A., and Mulder, T., 1996, The Himalayan foreland basin, *in* Yin, A., and Harrison, T.M., eds., The Tectonics of Asia: New York, Cambridge University Press, p. 149–188.

Calvès, G., Huuse, M., Clift, P.D., and Brusset, S., 2015, Giant fossil mass wasting off the coast of West India: The Nataraja submarine slide: Earth and Planetary Science Letters, v. 432, p. 265–272, https://doi.org/10.1016/j.epsl.2015.10.022.

Canfield, D.E., Raiswell, R., and Bottrell, S.H., 1992, The reactivity of sedimentary iron minerals toward sulfide: American Journal of Science, v. 292, p. 659–683, https://doi.org/10.2475/ajs.292.9.659.

Caves, J.K., Jost, A.B., Lau, K.V., and Maher, K., 2016, Cenozoic carbon cycle imbalances and a variable weathering feedback: Earth and Planetary Science Letters, v. 450, p. 152–163, https://doi.org/10.1016/j.epsl.2016.06.035.

Caves Rugenstein, J.K., Ibarra, D.E., and von Blanckenburg, F., 2019, Neogene cooling driven by land surface reactivity rather than increased weathering fluxes: Nature, v. 571, p. 99–102, https://doi.org/10.1038/s41586-019-1332-y.

Chamley, H., 1989, Clay formation through weathering, *in* Clay Sedimentology: Berlin, Heidelberg, Springer-Verlag, p. 21–50, https://doi.org/10.1007/978-3-642-85916-8_2.

Clemens, S.C., and Prell, W.L., 2003, A 350,000 year summer-monsoon multi-proxy stack from the Owen Ridge, Northern Arabian Sea: Marine Geology, v. 201, p. 35–51, https://doi.org/10.1016/S0025-3227(03)00207-X.

Clemens, S.C., and Prell, W.L., 2007, The timing of orbital-scale Indian monsoon changes: Quaternary Science Reviews, v. 26, p. 275–278, https://doi.org/10.1016/j.quascirev.2006.11.010.

Clift, P.D., 2006, Controls on the erosion of Cenozoic Asia and the flux of clastic sediment to the ocean: Earth and Planetary Science Letters, v. 241, p. 571–580, https://doi.org/10.1016/j.epsl.2005.11.028.

Clift, P.D., 2017, Cenozoic sedimentary records of climate-tectonic coupling in the Western Himalaya: Progress in Earth and Planetary Science, v. 4, https://doi.org/10.1186/s40645-017-0151-8.

Clift, P.D., and Giosan, L., 2014, Sediment fluxes and buffering in the post-glacial Indus Basin: Basin Research, v. 26, p. 369–386, https://doi.org/10.1111/bre.12038.

Clift, P.D., Shimizu, N., Layne, G.D., Blusztajn, J.S., Gaedicke, C., Schlüter, H.-U., Clark, M.K., and Amjad, S., 2001, Development of the Indus Fan and its significance for the erosional history of the Western Himalaya and Karakoram: Geological Society of America Bulletin, v. 113, p. 1039–1051, https://doi.org/10.1130/0016-7606(2001)113<1039:DOTIFA>2.0.CO;2.

Clift, P.D., Lee, J.I., Hildebrand, P., Shimizu, N., Layne, G.D., Blusztajn, J., Blum, J.D., Garzanti, E., and Khan, A.A., 2002, Nd and Pb isotope variability in the Indus River System: Implications for sediment provenance and crustal heterogeneity in the Western Himalaya: Earth and Planetary Science Letters, v. 200, p. 91–106, https://doi.org/10.1016/S0012-821X(02)00620-9.

Clift, P.D., Giosan, L., Blusztajn, J., Campbell, I.H., Allen, C., Pringle, M., Tabrez, A.R., Danish, M., Rabbani, M.M., Alizai, A., Carter, A., and Lückge, A., 2008a, Holocene erosion of the Lesser Himalaya triggered by intensified summer monsoon: Geology, v. 36, p. 79–82, https://doi.org/10.1130/G24315A.1.

Clift, P.D., Hodges, K.V., Heslop, D., Hannigan, R., Hoang, L.V., and Calves, G., 2008b, Correlation of Himalayan exhumation rates and Asian monsoon intensity: Nature Geoscience, v. 1, p. 875–880, https://doi.org/10.1038/ngeo351.

Clift, P.D., Giosan, L., Carter, A., Garzanti, E., Galy, V., Tabrez, A.R., Pringle, M., Campbell, I.H., France-Lanord, C., Blusztajn, J., Allen, C., Alizai, A., Lückge, A., Danish, M., and Rabbani, M.M., 2010, Monsoon control over erosion patterns in the Western Himalaya: Possible feed-back into the tectonic evolution, *in* Clift, P.D., Tada, R., and Zheng, H., eds., Monsoon Evolution and Tectonics-Climate Linkage in Asia: Geological Society of London Special Publication 342, p. 185–218, https://doi.org/10.1144/SP342.12.

Clift, P.D., Wan, S., and Blusztajn, J., 2014, Reconstructing chemical weathering, physical erosion and monsoon intensity since 25 Ma in the northern South China Sea: A review of competing proxies: Earth-Science Reviews, v. 130, p. 86–102, https://doi.org/10.1016/j.earscirev.2014.01.002.

Clift, P.D., Kulhanek, D.K., Zhou, P., Bowen, M.G., Vincent, S.M., Lyle, M., and Hahn, A., 2019a, Chemical weathering and erosion responses to changing monsoon climate in the Late Miocene of Southwest Asia: Geological Magazine, v. 157, p. 939–955, https://doi.org/10.1017/S0016756819000608.

Clift, P.D., Zhou, P., Stockli, D.F., and Blusztajn, J., 2019b, Regional Pliocene exhumation of the Lesser Himalaya in the Indus drainage: Solid Earth, v. 10, p. 647–661, https://doi.org/10.5194/se-10-647-2019.

Coleman, M.L., Hedrick, D.B., Lovley, D.R., White, D.C., and Pye, K., 1993, Reduction of Fe(III) in sediments by sulphate-reducing bacteria: Nature, v. 361, p. 436–438, https://doi.org/10.1038/361436a0.

Colin, C., Turpin, L., Bertaux, J., Desprairies, A., and Kissel, C., 1999, Erosional history of the Himalayan and Burman ranges during the last two glacial-interglacial cycles: Earth and Planetary Science Letters, v. 171, p. 647–660, https://doi.org/10.1016/S0012-821X(99)00184-3.

Curry, W.B., Ostermann, D.R., Guptha, M.V.S., and Itekkot, V., 1992, Foraminiferal production and monsoonal upwelling in the Arabian Sea: Evidence from sediment traps, *in* Summerhayes, C.P., Prell, W.L., and Emeis, K.C., eds., Upwelling Systems: Evolution Since the Early Miocene: Geological Society of London Special Publication 64, p. 93–106, https://doi.org/10.1144/GSL.SP.1992.064.01.06.

Dailey, S.K., Clift, P.D., Kulhanek, D.K., Blusztajn, J., Routledge, C.M., Calvès, G., O'Sullivan, P., Jonell, T.N., Pandey, D.K., Andò, S., Coletti, G., Zhou, P., Li, Y., Neubeck, N.E., Bendle, J.A.P., Ahranovich, S., Griffith, E.M., Gurumurthy, G.P., Hahn, A., Iwai, M., Khim, B.-K., Kumar, A., Kumar, A.G., Liddy, H.M., Lu, H., Lyle, M.W., Mishra, R., Radhakrishna, T., Saraswat, R., Saxena, R., Scardia, G., Sharma, G.K., Singh, A.D., Steinke, S., Suzuki, K., Tauxe, L., Tiwari, M., Xu, Z., and Yu, Z., 2019, Large-scale mass wasting on the Miocene continental margin of western India: Geological Society of America Bulletin, v. 132, p. 85–122, https://doi.org/10.1130/B35158.1.

Deaton, B.C., and Balsam, W.L., 1991, Visible spectroscopy—A rapid method for determining hematite and goethite concentration in geological materials: Journal of Sedimentary Research, v. 61, p. 628–632, https://doi.org/10.1306/D4267794-2B26-11D7-8648000102C1865D.

DeCelles, P.G., Kapp, P., Gehrels, G.E., and Ding, L., 2014, Paleocene-Eocene foreland basin evolution in the Himalaya of southern Tibet and Nepal: Implications for the age of initial India-Asia collision: Tectonics, v. 33, p. 824–849, https://doi.org/10.1002/2014TC003522.

Dekkers, M.J., 1978, Magnetic properties of sediments, *in* Fairbridge, R.W., ed., Sedimentology: Berlin, Heidelberg, Springer, Encyclopedia of Earth Science Series, p. 684–692, https://doi.org/10.1007/3-540-31079-7_130.

Demske, D., Tarasov, P.E., Wünnemann, B., and Riedel, F., 2009, Late glacial and Holocene vegetation, Indian monsoon and westerly circulation in the Trans-Himalaya recorded in the lacustrine pollen sequence from Tso Kar, Ladakh, NW India: Palaeogeography, Palaeoclimatology, Palaeoecology, v. 279, p. 172–185, https://doi.org/10.1016/j.palaeo.2009.05.008.

DePaolo, D.J., and Wasserburg, G.J., 1976, Nd isotopic variations and petrogenetic models: Geophysical Research Letters, v. 3, p. 249–252, https://doi.org/10.1029/GL003i005p00249.

Dettman, D.L., Kohn, M.J., Quade, J., Ryerson, F.J., Ojha, T.P., and Hamidullah, S., 2001, Seasonal stable isotope evidence for a strong Asian monsoon throughout the past 10.7 m.y.: Geology, v. 29, p. 31–34, https://doi.org/10.1130/0091-7613(2001)029<0031:SSIEFA>2.0.CO;2.

Dickinson, W.R., and Suczek, C.A., 1979, Plate tectonics and sandstone compositions: American Association of Petroleum Geologists Bulletin, v. 63, p. 2164–2182, https://doi.org/10.1306/2F9188FB-16CE-11D7-8645000102C1865D.

Ding, L., Qasim, M., Jadoon, I.A.K., Khan, M.A., Xu, Q., Cai, F., Wang, H., Baral, U., and Yue, Y., 2016, The India-Asia collision in north Pakistan: Insight from the U-Pb detrital zircon provenance of Cenozoic foreland basin: Earth and Planetary Science Letters, v. 455, p. 49–61, https://doi.org/10.1016/j.epsl.2016.09.003.

Dosseto, A., Bourdon, B., and Turner, S.P., 2008, Uranium-series isotopes in river materials: Insights into the timescales of erosion and sediment transport: Earth and Planetary Science Letters, v. 265, p. 1–17, https://doi.org/10.1016/j.epsl.2007.10.023.

Dosseto, A., Vigier, N., Joannes-Boyau, R., Moffat, I., Singh, T., and Srivastava, P., 2015, Rapid response of silicate weathering rates to climate change in the Himalaya: Geochemical Perspectives Letters, v. 1, p. 10–19, https://doi.org/10.7185/geochemlet.1502.

Dunlea, A.G., Murray, R.W., Sauvage, J., Spivack, A.J., Harris, R.N., and D'Hondt, S., 2015, Dust, volcanic ash, and the evolution of the South Pacific Gyre through the Cenozoic: Paleoceanography, v. 30, p. 1078–1099, https://doi.org/10.1002/2015PA002829.

East, A.E., Clift, P.D., Carter, A., Alizai, A., and VanLaningham, S., 2015, Fluvial-eolian interactions in sediment routing and sedimentary signal buffering: An example from the Indus Basin and Thar Desert: Journal of Sedimentary Research, v. 85, p. 715–728, https://doi.org/10.2110/jsr.2015.42.

Fedo, C.M., Nesbitt, H.W., and Young, G.M., 1995, Unraveling the effects of potassium metasomatism in sedimentary rocks and paleosols, with implications for paleoweathering conditions and provenance: Geology, v. 23, p. 921–924, https://doi.org/10.1130/0091-7613(1995)023<0921:UTEOPM>2.3.CO;2.

France-Lanord, C., Spiess, V., Klaus, A., Schwenk, T., and Expedition 354 Scientists, 2016, Bengal Fan: Proceedings of the International Ocean Discovery Program, Volume 354: College Station, Texas, International Ocean Discovery Program, https://doi.org/10.14379/iodp.proc.354.2016.

Galy, V., France-Lanord, C., Beyssac, O., Faure, P., Kudrass, H., and Palhol, F., 2007, Efficient organic carbon burial in the Bengal fan sustained by the Himalayan erosional system: Nature, v. 450, p. 407–410, https://doi.org/10.1038/nature06273.

Garzanti, E., and Andò, S., 2007, Heavy mineral concentration in modern sands: Implications for provenance interpretation, *in* Mange, M.A., and Wright, D.T., eds., Heavy Minerals in Use: Amsterdam, Elsevier, Developments in Sedimentology, v. 58, p. 517–545, https://doi.org/10.1016/S0070-4571(07)58020-9.

Garzanti, E., Baud, A., and Mascle, G., 1987, Sedimentary record of the northward flight of India and its collision with Eurasia (Ladakh Himalaya, India): Geodinamica Acta, v. 1, p. 297–312, https://doi.org/10.1080/09853111.1987.11105147.

Garzanti, E., Vezzoli, G., Andò, S., France-Lanord, C., Singh, S.K., and Foster, G., 2004, Sand petrology and focused erosion in collision orogens: The Brahmaputra case: Earth and Planetary Science Letters, v. 220, p. 157–174, https://doi.org/10.1016/S0012-821X(04)00035-4.

Garzanti, E., Vezzoli, G., Andò, S., Paparella, P., and Clift, P.D., 2005, Petrology of Indus River sands: A key to interpret erosion history of the Western Himalayan Syntaxis: Earth and Planetary Science Letters, v. 229, no. 3–4, p. 287–302, https://doi.org/10.1016/j.epsl.2004.11.008.

Gingele, F.X., Müller, P.M., and Schneider, R.R., 1998, Orbital forcing of freshwater input in the Zaire Fan area—Clay mineral evidence from the last 200 kyr: Palaeogeography, Palaeoclimatology, Palaeoecology, v. 138, p. 17–26, https://doi.org/10.1016/S0031-0182(97)00121-1.

Gingele, F.X., De Deckker, P., and Hillenbrand, C.-D., 2001, Clay mineral distribution in surface sediments between Indonesia and NW Australia—Source and transport by ocean currents: Marine Geology, v. 179, p. 135–146, https://doi.org/10.1016/S0025-3227(01)00194-3.

Giosan, L., Flood, R.D., and Aller, R.C., 2002a, Paleoceanographic significance of sediment color on western North Atlantic drifts: I. Origin of color: Marine Geology, v. 189, p. 25–41, https://doi.org/10.1016/S0025-3227(02)00321-3.

Giosan, L., Flood, R.D., Grutzner, J., and Mudie, P., 2002b, Paleoceanographic significance of sediment color on western North Atlantic Drifts: II. Late Pliocene–Pleistocene sedimentation: Marine Geology, v. 189, p. 43–61, https://doi.org/10.1016/S0025-3227(02)00322-5.

Goudie, A.S., and Viles, H.A., 2012, Weathering and the global carbon cycle: Geomorphological perspectives: Earth-Science Reviews, v. 113, p. 59–71, https://doi.org/10.1016/j.earscirev.2012.03.005.

Gupta, A.K., and Thomas, E., 2003, Initiation of Northern Hemisphere glaciation and strengthening of the northeast Indian monsoon: Ocean Drilling Program Site 758, eastern equatorial Indian Ocean: Geology, v. 31, p. 47–50, https://doi.org/10.1130/0091-7613(2003)031<0047:IONHGA>2.0.CO;2.

Gupta, A.K., Yuvaraja, A., Prakasam, M., Clemens, S.C., and Velu, A., 2015, Evolution of the South Asian monsoon wind system since the late Middle Miocene: Palaeogeography, Palaeoclimatology, Palaeoecology, v. 438, p. 160–167, https://doi.org/10.1016/j.palaeo.2015.08.006.

Heller, F., and Evans, M.E., 1995, Loess magnetism: Reviews of Geophysics, v. 33, p. 211–240, https://doi.org/10.1029/95RG00579.

Hillier, S., 1995, Erosion, sedimentation and sedimentary origin of clays, *in* Velde, B., ed., Origin and Mineralogy of Clays: Berlin, Heidelberg, Springer Verlag, p. 162–219, https://doi.org/10.1007/978-3-662-1013 12648-6_4.

Honjo, S., Dymond, J., Prell, W., and Ittekkot, V., 1999, Monsoon controlled export fluxes to the interior of the Arabian Sea: Deep-Sea Research: Part II, Topical Studies in Oceanography, v. 46, p. 1859–1902, https://doi.org/10.1016/S0967-0645(99)00047-8.

Hu, D., Clift, P.D., Wan, S., Böning, P., Hannigan, R., Hillier, S., and Blusztajn, J., 2016, Testing chemical weathering proxies in Miocene–Recent fluvial-derived sediments in the South China Sea, *in* Clift, P.D., Harff, J., Wu, J., and Qiu, Y., eds., River-Dominated Shelf Sediments of East Asian Seas: Geological Society of London Special Publication 429, p. 45–72, https://doi.org/10.1144/SP429.5.

Huyghe, P., Galy, A., Mugnier, J.-L., and France-Lanord, C., 2001, Propagation of the thrust system and erosion in the Lesser Himalaya: Geochemical and sedimentological evidence: Geology, v. 29, p. 1007–1010, https://doi.org/10.1130/0091-7613(2001)029<1007:POTTSA>2.0.CO;2.

Immerzeel, W.W., van Beek, L.P.H., and Bierkens, M.F.P., 2010, Climate change will affect the Asian water towers: Science, v. 328, p. 1382–1385, https://doi.org/10.1126/science.1183188.

Jagoutz, O., Macdonald, F.M., and Royden, L., 2016, Low-latitude arc-continent collision as a driver for global cooling: Proceedings of the National Academy of Sciences of the United States of America, v. 113, p. 4935–4940, https://doi.org/10.1073/pnas.1523667113.

Ji, J., Balsam, W., Chen, J.U., and Liu, L., 2002, Rapid and quantitative measurement of hematite and goethite in the Chinese loess-paleosol sequence by diffuse reflectance spectroscopy: Clays and Clay Minerals, v. 50, p. 208–216, https://doi.org/10.1346/000986002760832801.

Jonell, T.N., Owen, L.A., Carter, A., Schwenniger, J.-L., and Clift, P.D., 2017, Quantifying episodic erosion and transient storage on the western margin of the Tibetan Plateau, upper Indus River: Quaternary Research, v. 89, p. 281–306, https://doi.org/10.1017/qua.2017.92.

Jonell, T.N., Li, Y., Blusztajn, J., Giosan, L., and Clift, P.D., 2018, Signal or noise? Isolating grain size effects on Nd and Sr isotope variability in Indus delta sediment provenance: Chemical Geology, v. 485, p. 56–73, https://doi.org/10.1016/j.chemgeo.2018.03.036.

Karim, A., and Veizer, J., 2002, Water balance of the Indus River Basin and moisture source in the Karakoram and western Himalayas: Implications from hydrogen and oxygen isotopes in river water: Journal of Geophysical Research, v. 107, 4362, https://doi.org/10.1029/2000JD000253.

Khim, B.-K., Horikawa, K., Asahara, Y., Kim, J.-E., and Ikehara, M., 2019, Detrital Sr-Nd isotopes, sediment provenances and depositional processes in the Laxmi Basin of the Arabian Sea during the last 800 ka: Geological Magazine, v. 157, p. 895–907, https://doi.org/10.1017/S0016756818000596.

Kolla, V., and Coumes, F., 1987, Morphology, internal structure, seismic stratigraphy, and sedimentation of Indus Fan: American Association of Petroleum Geologists Bulletin, v. 71, p. 650–677, https://doi.org/10.1306/94887889-1704-11D7-8645000102C1865D.

Kroon, D., Steens, T., and Troelstra, S.R., 1991, Onset of monsoonal related upwelling in the western Arabian Sea as revealed by planktonic foraminifers, *in* Prell, W.L., and Niitsuma, N., eds., Proceedings of the Ocean Drilling Program, Scientific Results, Volume 117: College Station, Texas, Ocean Drilling Program, p. 257–263.

Kump, L.R., Brantley, S.L., and Arthur, M.A., 2000, Chemical weathering, atmospheric CO_2, and climate: Annual Review of Earth and Planetary Sciences, v. 28, p. 611–667, https://doi.org/10.1146/annurev.earth.28.1.611.

Kurian, S., Nath, B.N., Kumar, N.C., and Nair, K.K.C., 2013, Geochemical and isotopic signatures of surficial sediments from the western continental shelf of India: Inferring provenance, weathering, and the nature of organic matter geochemical and isotopic signatures of sediments from the Indian west coast: Journal of Sedimentary Research, v. 83, p. 427–442, https://doi.org/10.2110/jsr.2013.36.

Lamy, F., Hebbeln, D., and Wefer, G., 1998, Late Quaternary precessional cycles of terrigenous sediment input off the Norte Chico, Chile (27.5°S) and palaeoclimatic implications: Palaeogeography, Palaeoclimatology, Palaeoecology, v. 141, p. 233–251, https://doi.org/10.1016/S0031-0182(98)90052-9.

Lavé, J., and Avouac, J.P., 2000, Active folding of fluvial terraces across the Siwaliks Hills, Himalayas of central Nepal: Journal of Geophysical Research, v. 105, p. 5735–5770, https://doi.org/10.1029/1999JB900292.

Li, Y., 2018, Signal propagation, provenance, and climate records in the Indus Submarine Canyon since the Last Deglacial [Ph.D. thesis]: Baton Rouge, Louisiana State University, 188 p., https://digitalcommons.lsu.edu/gradschool_dissertations/4505.

Li, Y., Clift, P.D., Böning, P., Blusztajn, J., Murray, R.W., Ireland, T., Pahnke, K., Helm, N.C., and Giosan, L., 2018, Continuous signal propagation in the Indus Submarine Canyon since the last deglacial: Marine Geology, v. 406, p. 159–176, https://doi.org/10.1016/j.margeo.2018.09.011.

Li, Y., Clift, P.D., Murray, R.W., Exnicios, E., Ireland, T., and Böning, P., 2019, Asian summer monsoon influence on chemical weathering and sediment provenance determined by clay mineral analysis from the Indus Submarine Canyon: Quaternary Research, v. 93, p. 23–39, https://doi.org/10.1017/qua.2019.44.

Limmer, D., Köhler, C., Hillier, S., Mauqoy, D., Alizai, A., Sothcott, J., Giosan, L., Ponton, C., Tabrez, A., and Clift, P.D., 2012, Chemical weathering and provenance evolution of Holocene–recent sediments from the Western Indus Shelf, Northern Arabian Sea inferred from physical and mineralogical properties: Marine Geology, v. 326–328, p. 101–115, https://doi.org/10.1016/j.margeo.2012.07.009.

Liu, C., Clift, P.D., Giosan, L., Miao, Y., Warny, S., and Wan, S., 2019, Paleoclimatic evolution of the SW and NE South China Sea and its relationship with spectral reflectance data over various age scales: Palaeogeography, Palaeoclimatology, Palaeoecology, v. 525, p. 25–43, https://doi.org/10.1016/j.palaeo.2019.02.019.

Liu, Z., Colin, C., Trentesaux, A., Siani, G., Frank, N., Blamart, D., and Farid, S., 2005, Late Quaternary climatic control on erosion and weathering in the eastern Tibetan Plateau and the Mekong Basin: Quaternary Research, v. 63, p. 316–328, https://doi.org/10.1016/j.yqres.2005.02.005.

Lupker, M., France-Lanord, C., Galy, V., Lavé, J., Gaillardet, J., Gajurel, A.P., Guilmette, C., Rahman, M., Singh, S.K., and Sinha, R., 2012, Predominant floodplain over mountain weathering of Himalayan sediments (Ganga basin): Geochimica et Cosmochimica Acta, v. 84, p. 410–432, https://doi.org/10.1016/j.gca.2012.02.001.

Lupker, M., France-Lanord, C., Galy, V., Lavé, J., and Kudrass, H., 2013, Increasing chemical weathering in the Himalayan system since the Last Glacial Maximum: Earth and Planetary Science Letters, v. 365, p. 243–252, https://doi.org/10.1016/j.epsl.2013.01.038.

Macdonald, F.A., Swanson-Hysell, N.L., Park, Y., Lisiecki, L., and Jagoutz, O., 2019, Arc-continent collisions in the tropics set Earth's climate state: Science, v. 364, p. 181–184, https://doi.org/10.1126/science.aav5300.

Maclaren, M., 1906, III.—On the origin of certain laterites: Geological Magazine, v. 3, p. 536–547, https://doi.org/10.1017/S0016756800119004.

Miles, P.R., and Roest, W.R., 1993, Earliest sea-floor spreading magnetic anomalies in the north Arabian Sea and the ocean-continent transition: Geophysical Journal International, v. 115, p. 1025–1031, https://doi.org/10.1111/j.1365-246X.1993.tb01507.x.

Naini, B.R., and Kolla, V., 1982, Acoustic character and thickness of sediments of the Indus Fan and the continental margin of western India: Marine Geology, v. 47, p. 181–195, https://doi.org/10.1016/0025-3227(82)90068-8.

Nair, N., and Pandey, D.K., 2018, Cenozoic sedimentation in the Mumbai Offshore Basin: Implications for tectonic evolution of the western continental margin of India: Journal of Asian Earth Sciences, v. 152, p. 132–144, https://doi.org/10.1016/j.jseaes.2017.11.037.

Najman, Y., 2006, The detrital record of orogenesis: A review of approaches and techniques used in the Himalayan sedimentary basins: Earth-Science Reviews, v. 74, p. 1–72, https://doi.org/10.1016/j.earscirev.2005.04.004.

Najman, Y., Bickle, M., Garzanti, E., Pringle, M., Barfod, D., Brozovic, N., Burbank, D., and Ando, S., 2009, Reconstructing the exhumation history of the Lesser Himalaya, NW India, from a multitechnique provenance study of the foreland basin Siwalik Group: Tectonics, v. 28, TC5018, https://doi.org/10.1029/2009TC002506.

Najman, Y., Appel, E., Boudagher-Fadel, M., Bown, P., Carter, A., Garzanti, E., Godin, L., Han, J., Liebke, U., Oliver, G., Parrish, R., and Vezzoli, G., 2010, Timing of India-Asia collision: Geological, biostratigraphic, and palaeomagnetic constraints: Journal of Geophysical Research, v. 115, B12416, https://doi.org/10.1029/2010JB007673.

Nesbitt, H.W., Markovics, G., and Price, R.C., 1980, Chemical processes affecting alkalis and alkaline earths during continental weathering: Geochimica et Cosmochimica Acta, v. 44, p. 1659–1666, https://doi.org/10.1016/0016-7037(80)90218-5.

Pandey, D.K., Clift, P.D., Kulhanek, D.K., Andò, S., Bendle, J.A.P., Bratenkov, S., Griffith, E.M., Gurumurthy, G.P., Hahn, A., Iwai, M., Khim, B.-K., Kumar, A., Kumar, A.G., Liddy, H.M., Lu, H., Lyle, M.W., Mishra, R., Radhakrishna, T., Routledge, C.M., Saraswat, R., Saxena, R., Scardia, G., Sharma, G.K., Singh, A.D., Steinke, S., Suzuki, K., Tauxe, L., Tiwari, M., Xu, Z., and Yu, Z., 2016a, Site U1456, *in* Pandey, D.K., Clift, P.D., Kulhanek, D.K., and the Expedition 355 Scientists, Arabian Sea Monsoon: Proceedings of the International Ocean Discovery Program, Volume 355: College Station, Texas, International Ocean Discovery Program, https://doi.org/10.14379/iodp.proc.355.103.2016.

Pandey, D.K., Clift, P.D., Kulhanek, D.K., Andò, S., Bendle, J.A.P., Bratenkov, S., Griffith, E.M., Gurumurthy, G.P., Hahn, A., Iwai, M., Khim, B.-K., Kumar, A., Kumar, A.G., Liddy, H.M., Lu, H., Lyle, M.W., Mishra, R., Radhakrishna, T., Routledge, C.M., Saraswat, R., Saxena, R., Scardia, G., Sharma, G.K., Singh, A.D., Steinke, S., Suzuki, K., Tauxe, L., Tiwari, M., Xu, Z., and Yu, Z.,

2016b, Site U1457, *in* Pandey, D.K., Clift, P.D., Kulhanek, D.K., and the Expedition 355 Scientists, Arabian Sea Monsoon: Proceedings of the International Ocean Discovery Program, Volume 355: College Station, Texas, International Ocean Discovery Program, https://doi.org/10.14379/iodp.proc.355.104.2016.

Pandey, D.K., Clift, P.D., Kulhanek, D.K., Andò, S., Bendle, J.A.P., Bratenkov, S., Griffith, 1143 E.M., Gurumurthy, G.P., Hahn, A., Iwai, M., Khim, B.-K., Kumar, A., Kumar, A.G., Liddy, 1144 H.M., Lu, H., Lyle, M.W., Mishra, R., Radhakrishna, T., Routledge, C.M., Saraswat, R., 1145 Saxena, R., Scardia, G., 2016c, Expedition Summary, *in* Pandey, D.K., Clift, P.D., Kulhanek, D.K., and the Expedition 355 Scientists, Arabian Sea Monsoon: Proceedings of the International Ocean Discovery Program, Volume 355: College Station, Texas, International Ocean Discovery Program, https://doi.org/10.14379/iodp.proc.355.101.2016.

Pandey, O.P., Agrawal, P.K., and Negi, J.G., 1995, Lithospheric structure beneath Laxmi Ridge and late Cretaceous geodynamic events: Geo-Marine Letters, v. 15, p. 85–91, https://doi.org/10.1007/BF01275411.

Pease, P.P., Tchakerian, V.P., and Tindale, N.W., 1998, Aerosols over the Arabian Sea: Geochemistry and source areas for aeolian desert dust: Journal of Arid Environments, v. 39, p. 477–496, https://doi.org/10.1006/jare.1997.0368.

Prell, W.L., Murray, D.W., Clemens, S.C., and Anderson, D.M., 1992, Evolution and variability of the Indian Ocean summer monsoon: Evidence from the western Arabian Sea drilling program, *in* Duncan, R.A., Rea, D.K., Kidd, R.B., von Rad, U., and Weissel, J.K., eds., Synthesis of Results from Scientific Drilling in the Indian Ocean: American Geophysical Union Geophysical Monograph 70, p. 447–469, https://doi.org/10.1029/GM070p0447.

Quade, J., Cerling, T.E., and Bowman, J.R., 1989, Development of Asian monsoon revealed by marked ecological shift during the latest Miocene in northern Pakistan: Nature, v. 342, p. 163–166, https://doi.org/10.1038/342163a0.

Quadri, V.-u.-N., and Shuaib, S., 1986, Hydrocarbon prospects of southern Indus basin, Pakistan: AAPG Bulletin, v. 70, p. 730–747, https://doi.org/10.1306/94886344-1704-11D7-8645000102C1865D.

Rahaman, W., Wittmann, H., and von Blanckenburg, F., 2017, Denudation rates and the degree of chemical weathering in the Ganga River basin from ratios of meteoric cosmogenic ^{10}Be to stable ^{9}Be: Earth and Planetary Science Letters, v. 469, p. 156–169, https://doi.org/10.1016/j.epsl.2017.04.001.

Raymo, M.E., 1994, The initiation of northern hemisphere glaciation: Annual Review of Earth and Planetary Sciences, v. 22, p. 353–383, https://doi.org/10.1146/annurev.ea.22.050194.002033.

Raymo, M.E., and Ruddiman, W.F., 1992, Tectonic forcing of Late Cenozoic climate: Nature, v. 359, p. 117–122, https://doi.org/10.1038/359117a0.

Roberts, A.P., 2015, Magnetic mineral diagenesis: Earth-Science Reviews, v. 151, p. 1–47, https://doi.org/10.1016/j.earscirev.2015.09.010.

Routledge, C.M., Kulhanek, D.K., Tauxe, L., Scardia, G., Singh, A.D., Steinke, S., Griffith, E.M., and Saraswat, R., 2019, A revised chronostratigraphic framework for International Ocean Discovery Program Expedition 355 sites in Laxmi Basin, eastern Arabian Sea: Geological Magazine, v. 157, p. 961–978, https://doi.org/10.1017/S0016756819000104.

Sangode, S.J., and Bloemendal, J., 2004, Pedogenic transformation of magnetic minerals in Pliocene–Pleistocene palaeosols of the Siwalik Group, NW Himalaya, India: Palaeogeography, Palaeoclimatology, Palaeoecology, v. 212, p. 95–118, https://doi.org/10.1016/S0031-0182(04)00306-2.

Schwertmann, U., 1971, Transformation of hematite to goethite in soils: Nature, v. 232, p. 624–625, https://doi.org/10.1038/232624a0.

Selvaraj, K., and Chen, C.-T.A., 2006, Moderate chemical weathering of subtropical Taiwan: Constraints from solid-phase geochemistry of sediments and sedimentary rocks: The Journal of Geology, v. 114, p. 101–116, https://doi.org/10.1086/498102.

Shuaib, S.M., 1982, Geology and hydrocarbon potential of offshore Indus Basin, Pakistan: Geologic notes: American Association of Petroleum Geologists Bulletin, v. 66, p. 940–946, https://doi.org/10.1306/03B5A363-16D1-11D7-8645000102C1865D.

Singh, M., Sharma, M., and Tobschall, H.J., 2005, Weathering of the Ganga alluvial plain, northern India: Implications from fluvial geochemistry of the Gomati River: Applied Geochemistry, v. 20, p. 1–21, https://doi.org/10.1016/j.apgeochem.2004.07.005.

Singh, S., Parkash, B., Awasthi, A.K., and Kumar, S., 2011, Late Miocene record of palaeovegetation from Siwalik palaeosols of the Ramnagar sub-basin, India: Current Science, v. 100, p. 213–222.

Sjolte, J., and Hoffmann, G., 2014, Modelling stable water isotopes in monsoon precipitation during the previous interglacial: Quaternary Science Reviews, v. 85, p. 119–135, https://doi.org/10.1016/j.quascirev.2013.12.006.

Stephenson, B.J., Searle, M.P., Waters, D.J., and Rex, D.C., 2001, Structure of the Main Central Thrust zone and extrusion of the High Himalayan deep crustal wedge, Kishtwar-Zanskar Himalaya: Journal of the Geological Society, v. 158, p. 637–652, https://doi.org/10.1144/jgs.158.4.637.

Thiry, M., 2000, Palaeoclimatic interpretation of clay minerals in marine deposits: An outlook from the continental origin: Earth-Science Reviews, v. 49, p. 201–221, https://doi.org/10.1016/S0012-8252(99)00054-9.

Vecchi, G.A., Xie, S.-P., and Fischer, A.S., 2004, Ocean-atmosphere covariability in the western Arabian Sea: Journal of Climate, v. 17, p. 1213–1224, https://doi.org/10.1175/1520-0442(2004)017<1213:OCITWA>2.0.CO;2.

Vögeli, N., Najman, Y., van der Beek, P., Huyghe, P., Wynn, P.M., Govin, G., van der Veen, I., and Sachse, D., 2017, Lateral variations in vegetation in the Himalaya since the Miocene and implications for climate evolution: Earth and Planetary Science Letters, v. 471, p. 1–9, https://doi.org/10.1016/j.epsl.2017.04.037.

Walker, C.B., Searle, M.P., and Waters, D.J., 2001, An integrated tectonothermal model for the evolution of the High Himalaya in western Zanskar with constraints from thermobarometry and metamorphic modeling: Tectonics, v. 20, p. 810–833, https://doi.org/10.1029/2000TC001249.

Walker, T.R., 1967, Formation of red beds in modern and ancient deserts: Geological Society of America Bulletin, v. 78, p. 353–368, https://doi.org/10.1130/0016-7606(1967)78[353:FORBIM]2.0.CO;2.

Wan, S., Li, A., Clift, P.D., and Stuut, J.-B.W., 2007, Development of the East Asian monsoon: Mineralogical and sedimentologic records in the northern South China Sea since 20 Ma: Palaeogeography, Palaeoclimatology, Palaeoecology, v. 254, p. 561–582, https://doi.org/10.1016/j.palaeo.2007.07.009.

Wan, S., Clift, P.D., Zhao, D., Hovius, N., Munhoven, G., France-Lanord, C., Wang, Y., Xiong, Z., Huang, J., Yu, Z., Zhang, J., Ma, W., Zhang, G., Li, A., and Li, T., 2017, Enhanced silicate weathering of tropical shelf sediments exposed during glacial lowstands: A sink for atmospheric CO_2: Geochimica et Cosmochimica Acta, v. 200, p. 123–144, https://doi.org/10.1016/j.gca.2016.12.010.

Webb, A.A.G., 2013, Preliminary palinspastic reconstruction of Cenozoic deformation across the Himachal Himalaya (northwestern India): Geosphere, v. 9, p. 572–587, https://doi.org/10.1130/GES00787.1.

Webster, P.J., Magaña, V.O., Palmer, T.N., Shukla, J., Tomas, R.A., Yanai, M., and Yasunari, T., 1998, Monsoons: Processes, predictability, and the prospects for prediction: Journal of Geophysical Research, v. 103, p. 14,451–414,510, https://doi.org/10.1029/97JC02719.

West, A.J., Galy, A., and Bickle, M.J., 2005, Tectonic and climatic controls on silicate weathering: Earth and Planetary Science Letters, v. 235, p. 211–228, https://doi.org/10.1016/j.epsl.2005.03.020.

Wilson, S.A., 1997, Data compilation for USGS reference material BHVO-2, Hawaiian Basalt: U.S. Geological Survey Open-File Report, 2 p.

Wu, Y., Ding, W., Clift, P.D., Li, J., Yin, S., Fang, Y., and Ding, H., 2019, Sedimentary budget of the Northwest Sub-basin, South China Sea: Controlling factors and geological implications: International Geology Review, v. 62, p. 970–987, https://doi.org/10.1080/00206814.2019.1597392.

You, Y., Huber, M., Müller, R.D., Poulsen, C.J., and Ribbe, J., 2009, Simulation of the Middle Miocene Climate Optimum: Geophysical Research Letters, v. 36, L04702, https://doi.org/10.1029/2008GL036571.

Yu, Z., Colin, C., Wan, S., Saraswat, R., Song, L., Xu, Z., Clift, P., Lu, H., Lyle, M., Kulhanek, D., Hahn, A., Tiwari, M., Mishra, R., Miska, S., and Kumar, A., 2019, Sea level–controlled sediment transport to the eastern Arabian Sea over the past 600 kyr: Clay minerals and Sr-Nd isotopic evidence from IODP Site U1457: Quaternary Science Reviews, v. 205, p. 22–34, https://doi.org/10.1016/j.quascirev.2018.12.006.

Zachos, J., Pagani, M., Sloan, L., Thomas, E., and Billups, K., 2001, Trends, rhythms, and aberrations in global climate 65 Ma to present: Science, v. 292, p. 686–693, https://doi.org/10.1126/science.1059412.

Zachos, J.C., Dickens, G.R., and Zeebe, R.E., 2008, An early Cenozoic perspective on greenhouse warming and carbon-cycle dynamics: Nature, v. 451, p. 279–283, https://doi.org/10.1038/nature06588.

Zhang, Y.G., Ji, J., Balsam, W., Liu, L., and Chen, J., 2009, Mid-Pliocene Asian monsoon intensification and the onset of Northern Hemisphere glaciation: Geology, v. 37, p. 599–602, https://doi.org/10.1130/G25670A.1.

Zhou, P., Carter, A., Li, Y., and Clift, P.D., 2019, Slowing rates of regional exhumation in the western Himalaya: Fission track evidence from the Indus Fan: Geological Magazine, v. 157, p. 848–863, https://doi.org/10.1017/S001675681900092X.

Zhuang, G., Najman, Y., Tian, Y., Carter, A., Gemignani, L., Wijbrans, J., Jan, M.Q., and Khan, M.A., 2018, Insights into the evolution of the Hindu Kush–Kohistan–Karakoram from modern river sand detrital geo- and thermochronological studies: Journal of the Geological Society, v. 175, p. 934–948, https://doi.org/10.1144/jgs2018-007.